Electronic Supplementary Information to accompany:

Thermal- and Light-Induced Valence Tautomerism with a Concerted Spin Transition in an Iron Tris(diimine) Complex

Jett T. Janetzki,[a] *Dominic S. Brown,*[a] *Florian Daumann,*[b] *I. Haseena Ismail,*[a] *Robert W. Gable,*[a] *Moya A. Hay,*[a] *Roger J. Mulder,*[c] *Alyona A. Starikova,*[d] *Birgit Weber,*[b] *Marcus J. Giansiracusa,*[a] *and Colette Boskovic**[a]

[a] School of Chemistry, University of Melbourne, Victoria 3010, Australia

[b] Institute for Inorganic and Analytical Chemistry, Friedrich Schiller University Jena, Humboldtstraße 8, 07743 Jena, Germany

[c] CSIRO Manufacturing, Clayton, Victoria 3168, Australia

[d] Institute of Physical and Organic Chemistry, Southern Federal University, 344090, Rostov-on-Don, Russian Federation

*c.boskovic@unimelb.edu.au

Table of Contents

Experimental and Synthetic Methods

Synthesis

Manipulations performed under anaerobic conditions were done under a N_2 atmosphere on a Schlenk line or in an M-Braun glove box. Solvents were dried over molecular sieves (3 Å) for a minimum of 3 days and stored under N_2 on sieves until used. Molecular sieves were activated by heating at 300 °C for 48 hours and then cooled under vacuum. Solvents were degassed prior to use via 3 freeze-pump-thaw cycles. All chemicals purchased were of reagent grade or higher and used as received, except Bu_4NPF_6 and ferrocene which were purified from hot ethanol recrystallization and sublimation, respectively. Ph-BIAN was prepared as previously reported.[1]

[Zn(Ph-BIAN)$_3$](BPh$_4$)$_2$ (**1**). In air, a solution of $Zn(CH_3COO)_2{\cdot}2H_2O$ (0.060 g, 0.27 mmol) in MeOH (5 mL) was added dropwise to a suspension of Ph-BIAN (0.27 g, 0.81 mmol) in MeOH (25 mL), resulting in a clear yellow solution. The reaction was stirred for 1 hour at 60 °C, before filtering. A MeOH (5 mL) solution of $NaBPh_4$ (0.19 g, 0.56 mmol) was added dropwise, producing a yellow solid. The solid was collected by vacuum filtration, washed with MeOH and Et_2O and air dried to yield **1** as a yellow solid (0.33 g, 72%). Layering a saturated DCM solution with Et_2O yielded yellow crystals of **1**·3DCM suitable for X-ray diffraction. The crude product was recrystallized by dissolving 0.2 g in 12 mL DCE, filtering, and layering with 24 mL *i*Pr$_2$O, which after one week yielded a crystalline solid, analyzing as **1**·1.5DCE·1.5*i*Pr$_2$O. Anal. Calcd for $C_{132}H_{112}N_6B_2Cl_3O_{1.5}Zn$: C, 79.28; H, 5.65; N, 4.20. Found C, 79.35; H, 6.00; N, 4.09. Selected FT-IR data (ATR, cm^{-1}): 1661 (m), 1626 (s), 1583 (s), 1426 (s), 1284 (m), 952 (m), 695 (s), 540 (m). UV-Vis (MeCN) λ_{max} (ε): 380 nm (5050 mol^{-1} cm^{-1}).

[Co(Ph-BIAN)$_3$](BPh$_4$)$_2$ (**2**). In air, a solution of $CoCl_2{\cdot}6H_2O$ (0.048 g, 0.20 mmol) in MeOH (5 mL) was added dropwise to a suspension of Ph-BIAN (0.2 g, 0.6 mmol) in MeOH (25 mL). The solution rapidly changed color from orange to red. The reaction was stirred for 1 hour at 60 °C, before filtering. A MeOH (5 mL) solution of $NaBPh_4$ (0.14 g, 0.41 mmol) was added dropwise, followed by addition of H_2O (30 mL), producing a red solid. The solid was collected by vacuum filtration, washed with MeOH and Et_2O and air dried to yield **2** as an orange solid (0.27 g, 80%). Layering a saturated DCM solution with *i*Pr_2O yielded dark red block crystals of **2**·DCM·2*i*Pr_2O suitable for X-ray diffraction. The crude product was recrystallized by dissolving 0.2 g in 12 mL DCE, filtering, and layering with 24 mL *i*Pr_2O, which after one week yielded a crystalline solid, analyzing as **2**·DCE·1.6*i*Pr_2O. Anal. Calcd for $C_{131.6}H_{112.4}N_6B_2Cl_2O_{1.6}Co$: C, 80.85; H, 5.80; N, 4.30. Found C, 80.46; H, 6.19; N, 4.14. Selected FT-IR data (ATR, cm^{-1}): 1650 (m), 1620 (s), 1581 (s), 1480 (s), 1421 (m), 1285 (m), 1125 (m), 953 (m), 696 (s), 513 (m). UV-Vis (MeCN) λ_{max} (ε): 400 nm (8720 L mol^{-1} cm^{-1}.

[Mn(Ph-BIAN)₃](BPh₄)₂ (**3**). In air, a solution of $MnCl_2 \cdot 4H_2O$ (0.045 g, 0.23 mmol) in MeOH (5 mL) was added dropwise to a suspension of Ph-BIAN (0.23 g, 0.7 mmol) in MeOH (25 mL). The solution rapidly changed color from orange to red. The reaction was stirred for 1 hour at 60 °C, before filtering. A MeOH (5 mL) solution of $NaBPh_4$ (0.16 g, 0.47 mmol) was added dropwise, followed by addition of H_2O (30 mL), to produce a red solid. The solid was collected by vacuum filtration, washed with MeOH and Et_2O and air dried to yield **3** as an orange solid (0.24 g, 62%). Layering a saturated DCE solution with *i*Pr_2O yielded dark red block crystals of **3**·1.5*i*Pr_2O suitable for X-ray diffraction. The crude product was recrystallized by dissolving 0.2 g in 12 mL DCE, filtering, and layering with 24 mL *i*Pr_2O, which after one week yielded a crystalline solid, analyzing as **3**·0.4*i*Pr_2O. Anal. Calcd for $C_{122.4}H_{93.6}N_6B_2O_{0.4}Mn$: C, 84.91; H, 5.45; N, 4.85. Found C, 85.30; H, 5.75; N, 4.84. Selected FT-IR data (ATR, cm^{-1}): 1653 (m), 1622 (s), 1581 (s), 1480 (s), 1421 (m), 1248 (m), 1117 (m), 951 (m), 834 (s), 696 (s), 511 (m). UV-Vis (MeCN) λ_{max} (ε): 400 nm (5700 L mol^{-1} cm^{-1}).

[Fe(Ph-BIAN)₃](BPh₄)₂ (**4**). Under N_2, a solution of $FeCl_2 \cdot 4H_2O$ (0.03 g, 0.15 mmol) in MeOH (5 mL) was added dropwise to a suspension of Ph-BIAN (0.15 g, 0.45 mmol) in MeOH (25 mL). The solution rapidly changed color from orange to green. The reaction was stirred for 1 hour at 60 °C, before filtering. A MeOH (5 mL) solution of $NaBPh_4$ (0.1 g, 0.3 mmol) was added dropwise to produce a green solid. The suspension was then left at −18 °C for 24 hours. The precipitate was collected by vacuum filtration in air, washed with MeOH and Et_2O and air dried to yield **3** as green solid (0.21 g, 84%). Layering a saturated MeCN solution with $i$$Pr_2O$ under N_2 yielded dark green crystals of **4**·2$i$$Pr_2O$ suitable for X-ray diffraction. The crude product was recrystallized under N_2 by dissolving 0.2 g in 12 mL MeCN, filtering, and layering with 24 mL $i$$Pr_2O$, which after one week yielded a crystalline solid, analyzing as **4**·1.7$i$$Pr_2O$. Anal. Calcd for $C_{130.2}H_{111.8}N_6B_2O_{1.7}Fe$: C, 83.84; H, 6.04; N, 4.51. Found C, 84.18; H, 6.42; N, 4.64. Selected FT-IR data (ATR, cm^{-1}): 3054 (w), 2982 (w), 1753 (w), 1621 (m), 1581 (s), 1484 (s), 1418 (m), 1300 (m), 1051 (m), 830 (s), 699 (vs), 540 (s). UV-Vis (MeCN) λ_{max} (ε): 690 nm (12,000 L mol^{-1} cm^{-1}).

X-ray Data Collection and Structure Solution

Single X-ray diffraction data for **1**·3DCM and **3**·1.5$i$$Pr_2O$ were collected using a Rigaku XtaLAB Synergy X-ray Diffractometer System using Cu Kα (λ = 1.5418 Å), while data for **2**·DCM·2$i$$Pr_2O$ and **4**·2$i$$Pr_2O$ were collected at the Australian Synchrotron MX2[2] and MX1[3] beamlines, respectively, tuned to approximate Mo-Kα radiation (λ = 0.71075 Å, MX1; λ = 0.71076 Å, MX2) fitted with a silicon double crystal monochromator. Data reduction for **1**·3DCM and **3**·1.5$i$$Pr_2O$ was carried out using CrysalisPro,[4] using gaussian absorption corrections while data reduction for **2**·DCM·2$i$$Pr_2O$ and **4**·2$i$$Pr_2O$ was performed using XDS, using medium multi-scan absorption correction in SADABS. Crystals of **4**·2$i$$Pr_2O$ were collected at multiple orientations and merged with SADABS.[5] Crystals were transferred directly from the mother liquor to crystallographic oil to prevent solvent loss and loss of crystallinity. All structures were solved with SHELXT[6] and refined using a full matrix least squared procedure based on F^2 using SHELXL within Olex2.[7,8] The solvent molecules in **1**·3DCM, **2**·DCM·2$i$$Pr_2O$, **3**·1.5$i$$Pr_2O$ and **4**·2$i$$Pr_2O$ were highly disordered and attempts to satisfactorily model the disorder were unsuccessful. Accordingly, the contribution of the solvent molecules to the structure was treated with the solvent mask routine[9] in Olex2, with the composition of the solvent molecules assigned based on the residual electron density and the volume of the solvent void. One BPh_4^- anion in **3**·1.5*i*Pr_2O was refined over two different orientations. All non-hydrogen atoms were refined using anisotropic displacement factors. Hydrogen atoms were placed at geometrical positions and refined using the riding model.

Powder X-ray diffraction (PXRD) data were measured on a Rigaku Synergy Dual Wavelength Rotating Anode X-ray Diffractometer System using Cu-Kα (λ = 1.5418 Å) at 100 K. Powder samples were prepared by crushing the sample gently and loading them into a borosilicate glass capillary for measurement. Data were collected at $2\theta = 50°$ with an exposure time of 60 seconds per frame and processed using CrysAlisPro.[4]

Infrared and UV-Vis-NIR Spectroscopy

Attenuated total reflectance infrared spectra were measured on a Bruker Alpha spectrometer and normalized as absorbance spectra. Samples for solution UV-Visible-NIR measurements were prepared in an M-Braun N_2-atmosphere glove box and placed in a gastight cuvette. Solution state UV-Visible-NIR spectra were measured on a PerkinElmer UV-Vis-NIR Spectrometer Lambda 1050. Solution state variable-temperature UV−visible absorption spectra were measured on an Agilent Cary UV−visible Multicell Peltier Spectrometer, with a flow of N_2 gas to remove condensation. Diffuse reflectance UV-Visible spectra were measured on the samples diluted ~5% in KBr on a Thermo Scientific Evolution 220 UV-Visible spectrophotometer. The NIR spectrum of the $[Co^{II}((Ph\text{-}BIAN^{\bullet-})(Ph\text{-}BIAN^{0})_2]^+$ state of **2** in DCM and MeCN was previously reported,[10] generated electrochemically in a transmission cell of Hartl design fitted with CaF_2 windows and controlled by the EmStat^{3+} from solutions of the analyte in 0.1 M NBu_4PF_6 and recorded on a Cary 5000 UV-Vis-NIR spectrometer.

Mössbauer Spectroscopy

Zero-field ^{57}Fe Mössbauer spectra were recorded in transmission geometry in constant acceleration mode on WissEl (Wissenschaftliche Elektronik GmbH) spectrometers, equipped with a ^{57}Co(Rh) source (Ritverc JSC) having a nominal activity of 50 mCi and a 10 mm active window (sealed by Be) that is kept at room temperature. The polycrystalline material was filled into polyetheretherketone (PEEK) containers, and PTFE-made disks were used to ensure homogeneous distribution of the sample within the containment. For low temperature spectra, the sample holder was mounted onto a copper block and inserted into a static exchange gas cryostat (CRYO Industries of America, Inc.) which is connected to a temperature controller from Lake Shore Cryotronics, Inc. Data acquisition at 300 K and above were conducted by filling the polycrystalline material into a boron nitride disk (WissEl) with an inner diameter of 13 mm which was fixated in a stainless steel holder and placed in a MBF-1100 furnace (WissEl) consisting of a quartz tube sealed by a mylar window (outer window) and a 0.15 mm thick aluminum foil as the inner heat screen on each side. The temperature was measured by a Chromel®-Alumel® thermocouple at the sample holder ensuring a temperature gradient of the sample of <5%. Precise temperature control (± 0.1 °C) is ensured via a temperature control unit from J-Kem Scientific (Model 410A). Incoming signals were detected with a proportional counter and cached in a multichannel analyzer (CMCA-550, operating in 512 channels). Counts were transferred to the Wissoft 2003[11] interface on a computer. Isomer shifts are reported relative to α-iron foil at 298 K (without correction in terms of the second-order Doppler shift). Suitable fit models were obtained using the Recoil software package.[12]

Solid-State Magnetic Measurements

The dc susceptibility and magnetization measurements for samples **2**·DCE·1.6*i*Pr$_2$O, **3**·0.4*i*Pr$_2$O and **4**·1.7*i*Pr$_2$O were performed on a Quantum Design MPMS3 SQUID magnetometer measured with an applied field of 1000 Oe. Compounds **2**·DCE·1.6*i*Pr_2O and **3**·0.4*i*Pr_2O were loaded into a gel cap (**2**·DCE·1.6*i*Pr_2O was restrained in eicosane) and measured between 1.8 and 300 K. Compound **4**·1.7*i*Pr_2O was loaded into a plastic cap and measured between 1.8 and 400 K. Measurements employed scan rates of 2 K/min for 20–400 K, 1 K/min for 10–19 K, and 0.5 K/min for 1.8–9 K. The data was corrected for the diamagnetic contribution of the plastic/gel cap, eicosane and of the sample using half the molar mass. Compound **4**·1.7*i*Pr_2O was measured from 300 to 1.8 K, before measuring to 400 K, followed by measurement to 1.8 K, followed by measurement to 400 K. Magnetization (M) vs field (H) measurements were performed between 0 and 7 T at 1.8, 4 and 7 K.

Photomagnetic Measurements

Photomagnetic measurements of **4**·1.7*i*Pr_2O were performed on a Quantum Design MPMS3 SQUID magnetometer, coupled to a TLS120Xe High Power Tuneable Light Source (280 – 1100 nm). Sample irradiation at UV-Vis wavelengths were performed using the UV-Vis fibre optic sample holder (FOSH) and fibre optic bundle. Sample irradiation at Vis-NIR wavelengths were performed using the Vis-NIR FOSH and fibre optic bundle. All photomagnetic measurements were performed in the DC scan mode, utilizing MultiView's Magneto-Optic option. The following parameters were used in the DC scan: 40 mm length in six seconds with one scan per measurement. The DC scans measured on warming followed photoirradiation employed a scan rate of 0.3 K min^{-1} across the full warming range (10–300 K). All measurements were performed in a 1 T field, with a center offset of 66.54 mm, and utilized a fixed range (1 V). All background scans were fitted with a power law, and the resulting fit used for the background subtraction:

$$0.000268531356291217 \cdot T^{-0.886570574983035} - 4 \times 10^{-5} \qquad \text{(eq. S1)}$$

where T is temperature. The diamagnetic contribution of **4**·1.7*i*Pr$_2$O was calculated as half the molar mass and subtracted from the background corrected magnetic susceptibility data. Compound **4**·1.7*i*Pr$_2$O (0.8 mg) was loaded into the UV-vis FOSH and irradiated with 420 nm light (bandwidth 19.2 nm) at 10 K for 12 hours. A background subtraction was performed by measuring the signal from the empty UV-vis FOSH in a 1 T field.

Solution-Based Magnetic Measurements

Solution-based magnetic susceptibility measurements were measured in MeCN for **2**, **3** and **4** by ^{1}H NMR spectroscopy according to Evans method.[13] Solution samples for **2** and **3** were prepared aerobically. The solution sample for **4** were prepared in an M-Braun N$_2$-atmosphere glove box and measured in an anaerobic NMR tube equipped with a J Young valve. A solvent mixture was prepared containing d$_3$-MeCN and 0.5−2% H$_3$-MeCN as a standard. Compounds **2**, **3** and **4** were dissolved in the solvent mixture to form a solution of precisely known concentration and placed inside an NMR tube. A narrow capillary was filled with the same solvent mixture and placed inside the NMR tube as an internal reference. Measurements for **2** and **3** were recorded at room temperature on a Burker Ascend 400 NMR spectrometer. Measurements for **4** were recorded between 238–328 K on a Bruker Av500 NMR spectrometer equipped with a 5 mm TCI CryoProbe Prodigy ^{1}H/^{2}H−^{13}C−^{15}N probe. Cooling was achieved with a Bruker BCU-II gas pre-conditioner. Sample temperature was calibrated using d$_4$-methanol and stable at ±0.1 K. The shift in the H$_3$-MeCN singlet in the paramagnetic solution compared to H$_3$−MeCN in the internal references, $\Delta\upsilon$ in hertz, can be used to calculate the mass susceptibility of the compound, χ_g:

$$\chi_g = \frac{3\Delta\upsilon}{4\pi m\upsilon} + \chi_0 + \chi_0\frac{d_0 - d_s}{m} \qquad \text{(eq. S2)}$$

where m is the concentration of the paramagnetic solution (in g cm^{-3}), corrected for the temperature dependence of the density of the solvent,[14,15] υ is the spectrometer frequency (in

Hz), χ_0 is the mass susceptibility of the solvent mixture, d_0 is the density of the pure solvent mixture, and d_s is the density of the compound solution. As the sample solution is dilute, the following approximation can be made: $d_s = d_s + m,$ leading to a cancelation of the second and third terms of eq. S3. The mass susceptibility is converted to the molar susceptibility by multiplying by the molecular weight (including molecules of solvation) and then corrected for the diamagnetic contribution of the compound using Pascal's constants.[16]

The $T_{1/2}$, ΔH and ΔS for **4** in MeCN were obtained by fitting $\chi_M T$ vs T data with the regular solution model:

$$\chi MT = (\chi MT)_{min} + \frac{(\chi MT)_{max} - (\chi MT)_{min}}{1 + e^{\frac{\Delta S}{R}\left(\frac{T_{\frac{1}{2}}}{T} - 1\right)}} \qquad \text{(eq. S3)}$$

where $(\chi_M T)_{\mathrm{min}}$ and $(\chi_M T)_{\mathrm{max}}$ are the minimum and maximum values of $\chi_M T$ respectively, and R is the ideal gas constant with a value of 8.314 J K^{-1} mol^{-1}.

Electrochemistry

Electrochemical measurements were performed in MeCN at room temperature using a standard three-electrode configuration connected to an eDAQ computer-controlled potentiostat. Measurements were performed under a constant flow of N_2. For cyclic voltammetry measurements, the three-electrode system consisted of a 1.0 mm diameter glassy carbon electrode (Cypress Systems), a platinum/titanium auxiliary electrode (eDAQ), and a Ag/AgCl reference electrode (eDAQ). For steady state voltammetry measurements, the working electrode was replaced with a 3.0 mm diameter glassy carbon rotating disk electrode with external controller (Metrohm). Analyte solutions of 1.0 mM were prepared using anaerobic techniques in 5 ml MeCN containing 0.25 M Bu_4NPF_6 as the supporting electrolyte. All potentials have been referenced *versus* the ferrocene/ferrocenium redox couple, measured immediately afterwards. The cyclic voltammetry (CV) midpoint potentials (E_m) are calculated by taking the average of the peak anodic potential (E_{pa}) and peak cathodic potential (E_{pc}). The peak-to-peal separation (ΔE_p) for a reversible process is calculated the difference of E_{pa} and E_{pc}. The ΔE_p values are close to the value measured under the same conditions for ferrocene at a scan rate of 100 mV s^{-1} (65–70 mV in MeCN). The half-wave potentials ($E_{1/2}$) are calculated as the potential at half the limiting current (i_L).

Elemental Analysis, Thermogravimetric Analysis

Elemental analyses (C, H, N) were performed at the Macquarie Analytical and Fabrication Facility, Macquarie University. Thermogravimetric analyses were performed on a Perkin Elmer TGA 8000 thermogravimetry analyzer using a ramp rate of 5 °C per minute from 30 °C up to a maximum temperature of 400 °C under an N_2 atmosphere.

Density Functional Theory Calculations

Density functional theory (DFT) calculations were performed for the cationic complexes of **2**, **3** and **4** in the gas phase to study the relative energy of the different electronic states. The electromer energies (E, kcal mol^{-1}) were calculated using the UTPSSh/6-311++G(d,p)[17,18] DFT method, which has been successful in modelling VT and SCO,[19–22] including Co-Ar-BIAN VT.[10] As UTPSSh/6-311++G(d,p) can over stabilizes LS-Fe(III/II)-containing species,[20,23] **4** was also calculated with UOPBE/6-311++G(d,p).[22,24–27] Calculations were performed on the cationic complex excluding the BPh_4^- anions to streamline computational time. The stationary points on the potential energy surface were located by full geometry optimization with subsequent confirmation of the stabilities of the DFT wave function and calculation of force constant matrices. The atomic coordinates obtained from experimental crystal structures of **2**, **3** and **4** were used as input files, excluding the counterions.

Literature Complexes

Chart S1. Representation of iron VT compounds listed in Table 1. For compounds [Fe(porphyrin)(thiolate)], the four porphyrin/thiolate ligands are shown beside the complex.

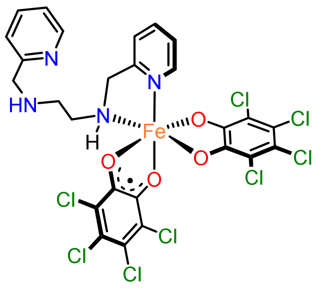

[Fe(bispicen)(Cl_4SQ)(Cl_4diox)]

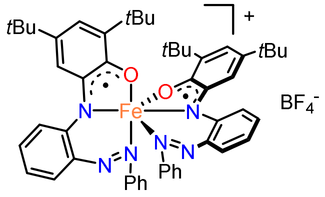

[Fe($paap)_2$](BF_4)

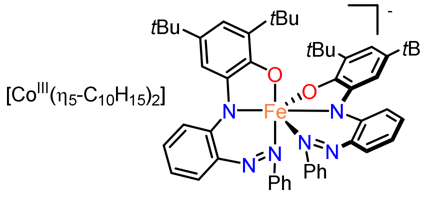

[Co^{III}(η_5-$C_{10}H_{15})_2$][Fe($paap)_2$]

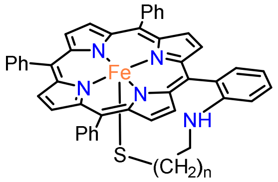

[Fe(porphyrin)(thiolate)]

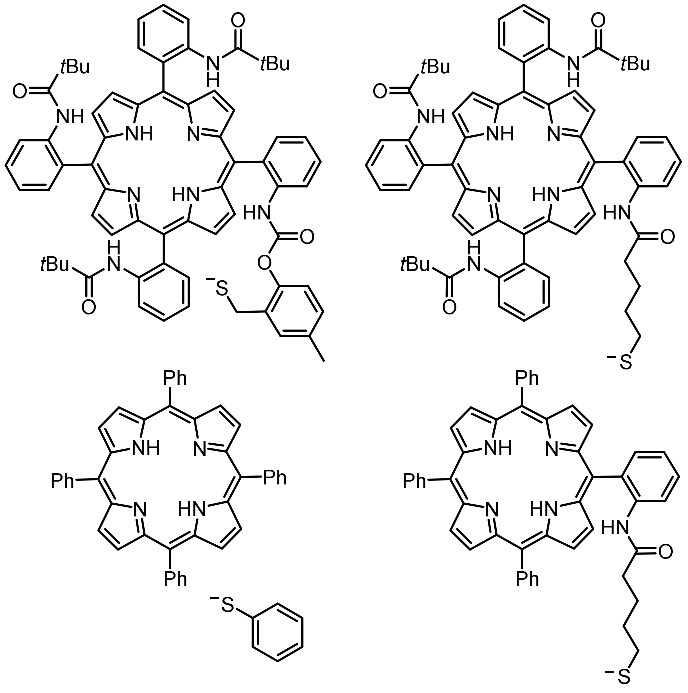

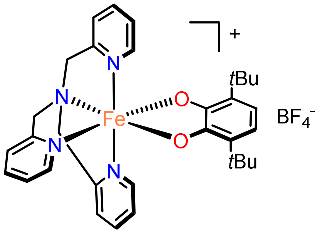

[Fe(tpa)(3,6-dbdiox)](BF_4)

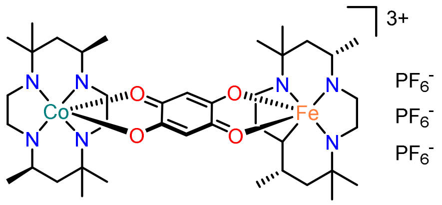

[(Fe(RR-cth)(Co(SS-cth)(DHBQ)]($PF_6)_3$

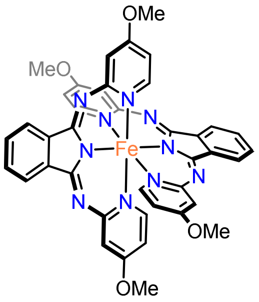

[Fe(4-MeO-bpi$)_2$]

Chart S2. Valence tautomeric equilibrium displayed by [Co(4-MeO-BIAN)$_3$] in solution.

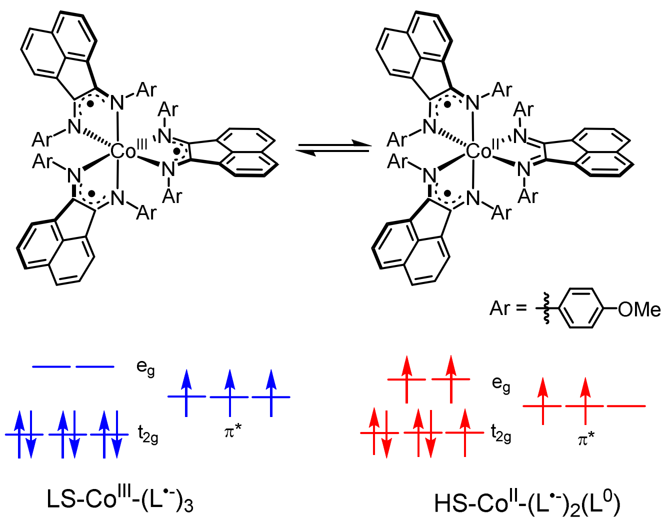

Thermogravimetric Analysis

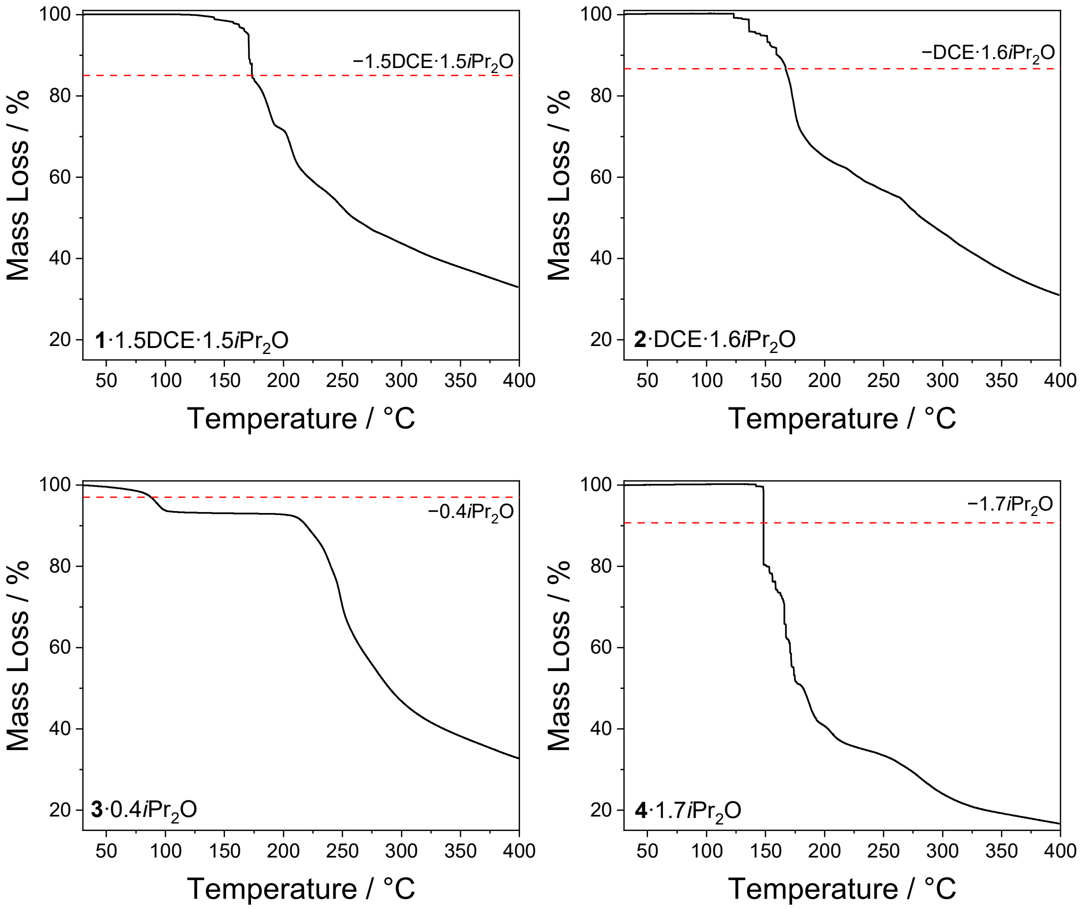

Figure S1. Thermogravimetric profile for **1**·1.5DCE·1.5*i*Pr_2O, **2**·DCE·1.6*i*Pr_2O, **3**·0.4*i*Pr_2O and **4**·1.7*i*Pr_2O under N_2 at a ramp rate of 5 °C min^{-1}.

Powder X-ray Diffraction

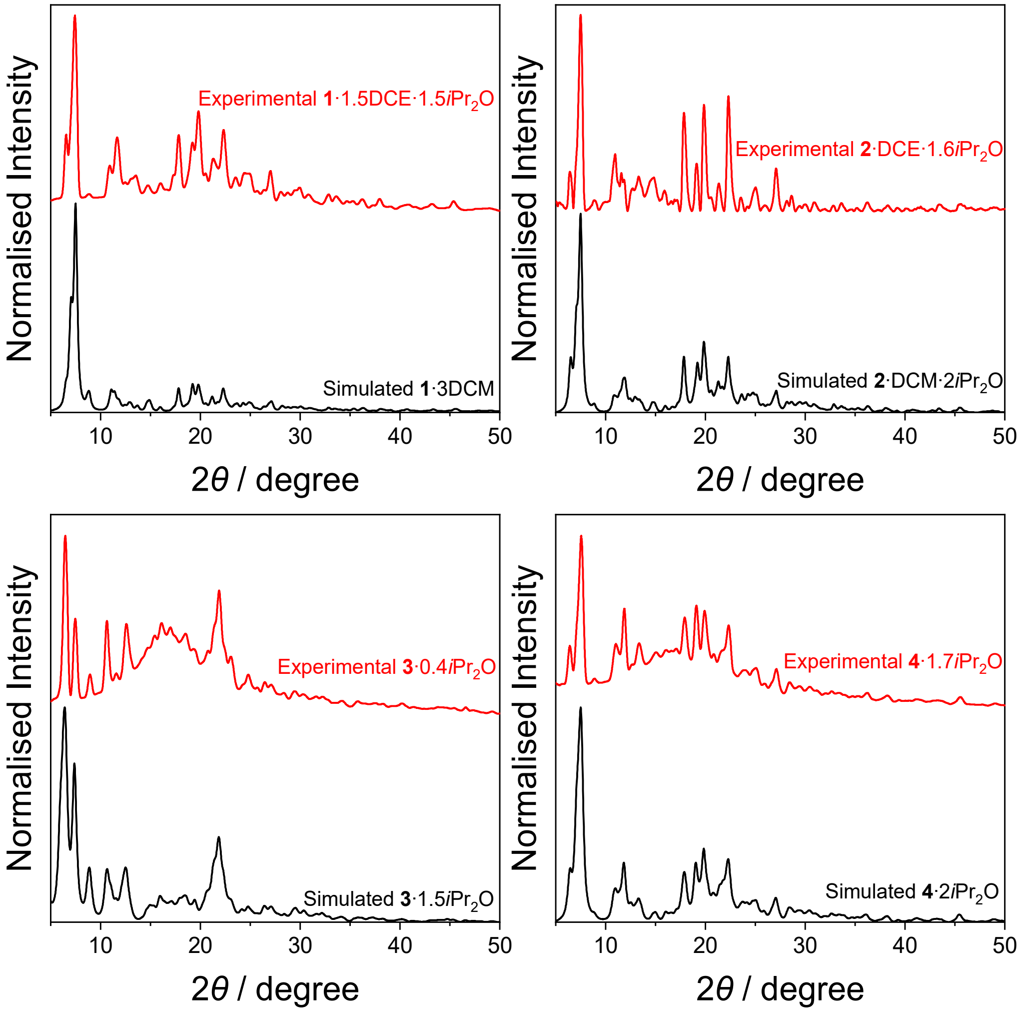

Figure S2. Top left: Experimental PXRD pattern of **1**·1.5DCE·1.5*i*Pr2O at 100 K (red) and simulated PXRD pattern from crystal structure of **1**·3DCM at 100 K (black). Top right: Experimental PXRD pattern of **2**·DCE·1.6*i*Pr2O at 100 K (red) and simulated PXRD pattern from crystal structure of **2**·DCM·2*i*Pr2O at 100 K (black). Bottom left: Experimental PXRD pattern of **3**·0.4*i*Pr2O at 100 K (red) and simulated PXRD pattern from crystal structure of **3**·1.5*i*Pr2O at 100 K (black). Bottom right: Experimental PXRD pattern of **4**·1.7*i*Pr2O at 100 K (red) and simulated PXRD pattern from crystal structure of **4**·2*i*Pr2O at 100 K (black).

Structural Data

Table S1. Crystallographic data and structure refinement parameters for compound **1**·3DCM, **2**·DCM·2*i*Pr$_2$O and **3**·1.5*i*Pr$_2$O at 100 K.

	1·3DCM	**2**·DCM·2*i*Pr$_2$O	**3**·1.5*i*Pr$_2$O
Empirical formula	$C_{123}H_{94}B_2Cl_6N_6Zn$	$C_{133}H_{118}B_2Cl_2CoN_6O_2$	$C_{129}H_{109}B_2MnN_6O_{1.5}$
Formula weight	1955.73	1983.78	1843.78
Temperature (K)	100.00(10)	100.00(2)	100.00(11)
Crystal system	monoclinic	monoclinic	triclinic
Space group	C2/c	C2/c	$P\bar{1}$
a (Å)	27.5951(2)	27.429(6)	17.0314(2)
b (Å)	13.48310(10)	13.479(3)	17.0463(3)
c (Å)	29.7605(2)	29.817(6)	21.0901(2)
α (°)	90	90	80.9160(10)
β (°)	114.5370(10)	114.30(3)	69.6040(10)
γ (°)	90	90	60.143(2)
Volume (Å^3)	10072.95(14)	10047(4)	4976.40(15)
Z	4	4	2
ρ_{calc} (g/cm^3)	1.290	1.311	1.230
μ (mm^{-1})	2.223	0.285	1.521
F(000)	4064.0	4180.0	1944.0
Crystal size (mm^3)	0.255 × 0.193 × 0.125	0.27 × 0.2 × 0.13	0.732 × 0.301 × 0.022
Radiation	Cu Kα (λ = 1.54184)	Synchrotron (λ = 0.71076)	Cu Kα (λ = 1.54184)
2θ range for data collection (°)	7.352 to 156.134	3.258 to 64.872	5.98 to 160.902
Index ranges	$-32 \le h \le 34$, $-17 \le k \le 16$, $-37 \le l \le 35$	$-40 \le h \le 40$, $-19 \le k \le 19$, $-37 \le l \le 38$	$-21 \le h \le 21$, $-21 \le k \le 21$, $-16 \le l \le 26$
Reflections collected	68269	104807	96120
Independent reflections	10656 [R_{int} = 0.0310, R_{sigma} = 0.0199]	14973 [R_{int} = 0.0711, R_{sigma} = 0.0403]	21372 [R_{int} = 0.0504, R_{sigma} = 0.0379]
Data/restraints/parameters	10656/0/584	14973/0/584	21372/210/1389
Goodness-of-fit on F^2	1.038	1.111	1.101
Final *R* indexes [$I \geq 2\sigma(I)$]	R_1 = 0.0348, wR_2 = 0.0964	R_1 = 0.0558, wR_2 = 0.1750	R_1 = 0.0428, wR_2 = 0.1128
Final *R* indexes [all data]	R_1 = 0.0367, wR_2 = 0.0978	R_1 = 0.0609, wR_2 = 0.1813	R_1 = 0.0488, wR_2 = 0.1181
Largest diff. peak/hole (e Å^{-3})	0.29/-0.32	0.72/-0.73	0.39/-0.41

Table S2. Crystallographic data and structure refinement parameters for compound **4**·2*i*Pr$_2$O at 100, 150, 200 and 250 K.

	4·2*i*Pr$_2$O (100 K)	**4**·2*i*Pr$_2$O (150 K)	**4**·2*i*Pr$_2$O (200 K)	**4**·2*i*Pr$_2$O (250 K)
Empirical formula	$C_{132}H_{116}B_2FeN_6O_2$	$C_{132}H_{116}B_2FeN_6O_2$	$C_{132}H_{116}B_2FeN_6O_2$	$C_{132}H_{116}B_2FeN_6O_2$
Formula weight	1895.77	1895.77	1895.77	1895.77
Temperature (K)	100.0(2)	150.0(2)	200.0(2)	250.0(2)
Crystal system	monoclinic	monoclinic	monoclinic	monoclinic
Space group	C2/c	C2/c	C2/c	C2/c
a (Å)	27.310(6)	27.350(6)	27.380(6)	27.440(6)
b (Å)	13.370(3)	13.400(3)	13.440(3)	13.470(3)
c (Å)	30.170(6)	30.240(6)	30.330(6)	30.390(6)
α (°)	90	90	90	90
β (°)	114.31(3)	114.19(3)	113.99(3)	113.83(3)
γ (°)	90	90	90	90
Volume (Å^3)	10039(4)	10109(4)	10197(4)	10275(4)
Z	4	4	4	4
ρ_{calc} (g/cm^3)	1.254	1.246	1.235	1.225
μ (mm^{-1})	0.210	0.209	0.207	0.205
F(000)	4008.0	4008.0	4008.0	4008.0
Crystal size (mm^3)	0.417 × 0.144 × 0.088	0.417 × 0.144 × 0.088	0.417 × 0.144 × 0.088	0.417 × 0.144 × 0.088
Radiation	Synchrotron (λ = 0.71075)	Synchrotron (λ = 0.71075)	Synchrotron (λ = 0.71075)	Synchrotron (λ = 0.71075)
2θ range for data collection (°)	2.962 to 58.452	2.954 to 58.414	2.94 to 58.568	2.93 to 58.68
Index ranges	$-34 \leq h \leq 35, -17 \leq k \leq 18, -40 \leq l \leq 40$	$-34 \leq h \leq 35, -18 \leq k \leq 18, -40 \leq l \leq 40$	$-34 \leq h \leq 35, -18 \leq k \leq 18, -40 \leq l \leq 38$	$-34 \leq h \leq 35, -18 \leq k \leq 18, -41 \leq l \leq 38$
Reflections collected	132131	131953	132654	134435
Independent reflections	12209 [R_{int} = 0.0377, R_{sigma} = 0.0163]	12229 [R_{int} = 0.0365, R_{sigma} = 0.0161]	12486 [R_{int} = 0.0339, R_{sigma} = 0.0158]	12544 [R_{int} = 0.0300, R_{sigma} = 0.0134]
Data/restraints/parameters	12209/0/584	12229/0/584	12486/0/584	12544/0/584
Goodness-of-fit on F^2	1.061	1.061	1.107	1.077
Final R indexes [$I \geq 2\sigma(I)$]	R_1 = 0.0400, wR_2 = 0.1084	R_1 = 0.0398, wR_2 = 0.1090	R_1 = 0.0391, wR_2 = 0.1099	R_1 = 0.0405, wR_2 = 0.1163
Final R indexes [all data]	R_1 = 0.0437, wR_2 = 0.1122	R_1 = 0.0440, wR_2 = 0.1142	R_1 = 0.0471, wR_2 = 0.1202	R_1 = 0.0454, wR_2 = 0.1222
Largest diff. peak/hole (e Å^{-3})	0.25/-0.41	0.28/-0.38	0.33/-0.35	0.30/-0.37

Table S3. Crystallographic data and structure refinement parameters for compound **4**·2*i*Pr_2O at 300, 350, 375 and 400 K.

	4·2*i*Pr_2O (300 K)	**4**·2*i*Pr_2O (350 K)	**4**·2*i*Pr_2O (375 K)	**4**·2*i*Pr_2O (400 K)
Empirical formula	$C_{132}H_{116}B_2FeN_6O_2$	$C_{132}H_{116}B_2FeN_6O_2$	$C_{132}H_{116}B_2FeN_6O_2$	$C_{132}H_{116}B_2FeN_6O_2$
Formula weight	1895.77	1895.77	1895.77	1895.77
Temperature (K)	300.0(2)	350.0(2)	375.0(2)	400.0(2)
Crystal system	monoclinic	monoclinic	monoclinic	monoclinic
Space group	C2/c	C2/c	C2/c	C2/c
a (Å)	27.510(6)	27.640(6)	27.710(6)	27.790(6)
b (Å)	13.520(3)	13.590(3)	13.640(3)	13.680(3)
c (Å)	30.450(6)	30.520(6)	30.550(6)	30.560(6)
α (°)	90	90	90	90
β (°)	113.67(3)	113.51(3)	113.46(3)	113.40(3)
γ (°)	90	90	90	90
Volume (Å^3)	10373(4)	10512(4)	10592(4)	10662(4)
Z	4	4	4	4
ρ_{calc} (g/cm^3)	1.214	1.198	1.189	1.181
μ (mm^{-1})	0.203	0.201	0.199	0.198
F(000)	4008.0	4008.0	4008.0	4008.0
Crystal size (mm^3)	0.417 × 0.144 × 0.088	0.417 × 0.144 × 0.088	0.417 × 0.144 × 0.088	0.417 × 0.144 × 0.088
Radiation	Synchrotron (λ = 0.71075)	Synchrotron (λ = 0.71075)	Synchrotron (λ = 0.71075)	Synchrotron (λ = 0.71075)
2θ range for data collection (°)	2.92 to 58.588	2.91 to 58.69	2.906 to 58.654	2.904 to 58.692
Index ranges	$-34 \leq h \leq 35$, $-18 \leq k \leq 18$, $-41 \leq l \leq 39$	$-34 \leq h \leq 36$, $-18 \leq k \leq 18$, $-41 \leq l \leq 39$	$-34 \leq h \leq 36$, $-18 \leq k \leq 18$, $-41 \leq l \leq 40$	$-33 \leq h \leq 36$, $-18 \leq k \leq 18$, $-41 \leq l \leq 39$
Reflections collected	136550	140022	141171	141625
Independent reflections	12698 [R_{int} = 0.0301, R_{sigma} = 0.0138]	12871 [R_{int} = 0.0330, R_{sigma} = 0.0141]	13005 [R_{int} = 0.0294, R_{sigma} = 0.0121]	13115 [R_{int} = 0.0297, R_{sigma} = 0.0127]
Data/restraints/parameters	12698/0/584	12871/0/584	13005/0/584	13115/0/584
Goodness-of-fit on F^2	1.074	1.073	1.085	1.042
Final R indexes [$I \geq 2\sigma(I)$]	R_1 = 0.0378, wR_2 = 0.1153	R_1 = 0.0398, wR_2 = 0.1208	R_1 = 0.0427, wR_2 = 0.1301	R_1 = 0.0459, wR_2 = 0.1389
Final R indexes [all data]	R_1 = 0.0429, wR_2 = 0.1203	R_1 = 0.0470, wR_2 = 0.1276	R_1 = 0.0551, wR_2 = 0.1435	R_1 = 0.0603, wR_2 = 0.1556
Largest diff. peak/hole (e Å^{-3})	0.20/-0.30	0.20/-0.27	0.20/-0.27	0.21/-0.28

Figure S3. Crystal images of **1**, **2**, **3** and **4** at 100 K.

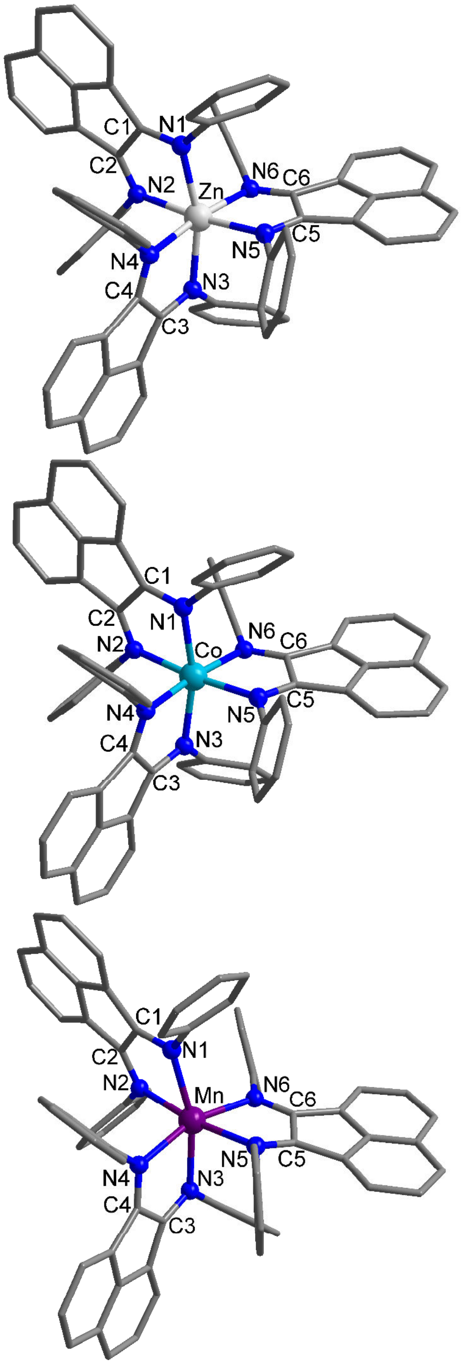

Figure S4. Cationic structure of **1**·3DCM (top), **2**·DCM·2*i*Pr$_2$O (middle), and **3**·1.5*i*Pr$_2$O (bottom) at 100 K with relevant atoms labelled. Hydrogen atoms, solvent molecules and BPh$_4^-$ anions have been omitted for clarity. Color code: C (dark grey), N (blue), Zn (light grey), Co (light blue), Mn (purple).

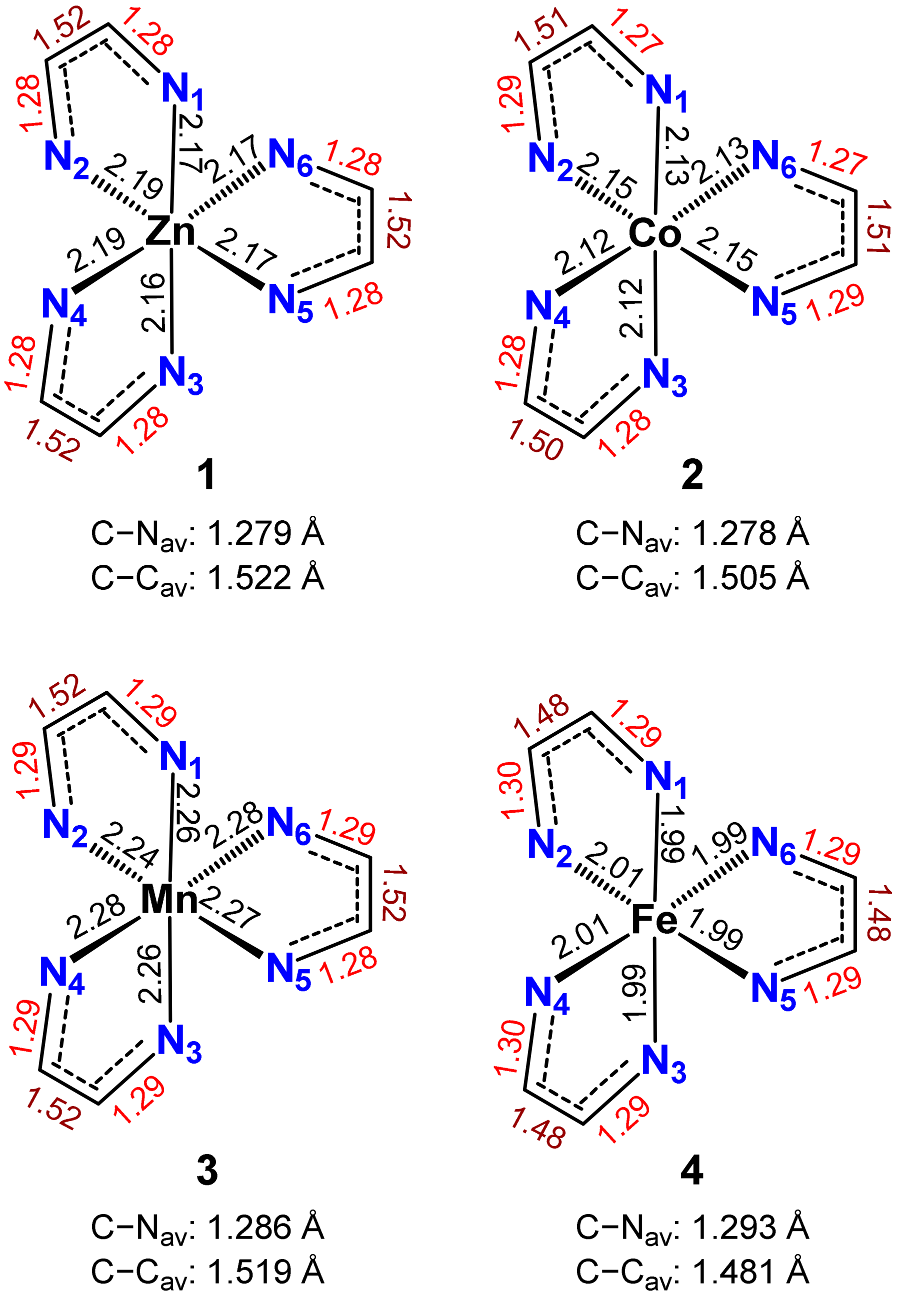

1

C−N$_{av}$: 1.279 Å
C−C$_{av}$: 1.522 Å

2

C−N$_{av}$: 1.278 Å
C−C$_{av}$: 1.505 Å

3

C−N$_{av}$: 1.286 Å
C−C$_{av}$: 1.519 Å

4

C−N$_{av}$: 1.293 Å
C−C$_{av}$: 1.481 Å

Figure S5. Comparison of bond lengths in **1**·3DCM, **2**·DCM·2*i*Pr$_2$O, **3**·1.5*i*Pr$_2$O and **4**·2*i*Pr$_2$O at 100 K.

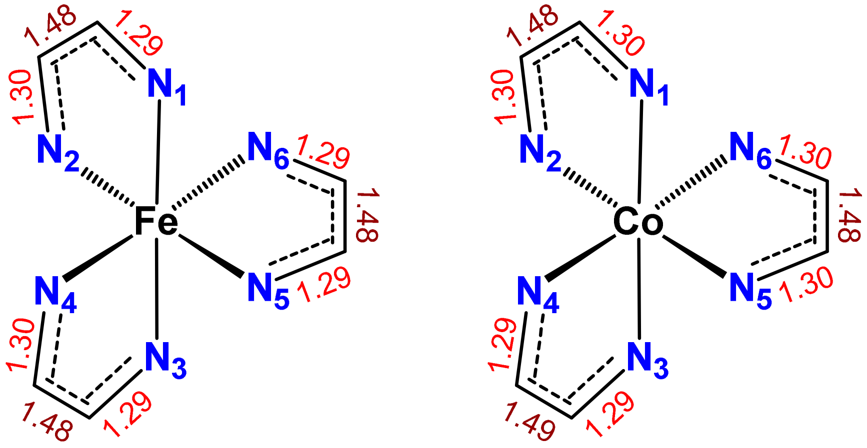

4

C−N$_{av}$: 1.293 Å
C−C$_{av}$: 1.481 Å

[Co^{II}(Ph-BIAN)$_3$]$^+$

C−N$_{av}$: 1.295 Å
C−C$_{av}$: 1.485 Å

Figure S6. Comparison of bond lengths in **4**·2*i*Pr$_2$O and [Co^{II}(Ph-BIAN^0)$_2$(Ph-BIAN$^{\bullet-}$)]$^+$at 100 K.[10]

Table S4. Selected Interatomic Distances (Å) and Distortion Parameters for **4**·2*i*Pr$_2$O.

	4·2*i*Pr$_2$O							
	100 K	150 K	200 K	250 K	300 K	350 K	375 K	400 K
Fe−N Interatomic Distances / Å								
Fe−N$_1$	1.991(2)	1.994(2)	1.995(1)	1.999(1)	2.000(1)	2.019(1)	2.039(1)	2.065(1)
Fe−N$_2$	2.008(2)	2.010(2)	2.011(2)	2.011(2)	2.013(1)	2.032(2)	2.050(2)	2.079(2)
Fe−N$_3$	1.991(2)	1.994(2)	1.995(1)	1.999(1)	2.000(1)	2.019(1)	2.039(1)	2.065(1)
Fe−N$_4$	2.008(2)	2.010(2)	2.011(2)	2.011(2)	2.013(1)	2.032(2)	2.050(2)	2.079(2)
Fe−N$_5$	1.991(2)	1.993(2)	1.994(1)	1.998(1)	2.000(1)	2.012(1)	2.034(1)	2.063(1)
Fe−N$_6$	1.991(2)	1.993(2)	1.994(1)	1.998(1)	2.000(1)	2.012(1)	2.034(1)	2.063(1)
Fe−N$_{av}$	1.997(5)	1.999(5)	2.000(3)	2.003(3)	2.004(2)	2.021(3)	2.041(3)	2.070(3)
C−N/C−C Interatomic Distances / Å								
C$_1$−N$_1$	1.292(3)	1.291(3)	1.293(2)	1.292(2)	1.294(2)	1.291(2)	1.286(2)	1.284(2)
C$_2$−N$_2$	1.295(3)	1.292(3)	1.298(2)	1.296(2)	1.294(2)	1.289(2)	1.295(2)	1.289(2)
C$_3$−N$_3$	1.292(3)	1.291(3)	1.293(2)	1.292(2)	1.294(2)	1.291(2)	1.286(2)	1.284(2)
C$_4$−N$_4$	1.295(3)	1.292(3)	1.298(2)	1.296(2)	1.294(2)	1.289(2)	1.295(2)	1.289(2)
C$_5$−N$_5$	1.292(3)	1.291(3)	1.293(2)	1.293(2)	1.289(2)	1.289(2)	1.283(2)	1.287(2)
C$_6$−N$_6$	1.292(3)	1.291(3)	1.293(2)	1.293(2)	1.289(2)	1.289(2)	1.283(2)	1.287(2)
C−N$_{av}$	1.293(7)	1.291(7)	1.295(5)	1.294(5)	1.292(5)	1.290(5)	1.288(5)	1.287(5)
C$_1$−C$_2$	1.482(3)	1.485(3)	1.482(3)	1.482(2)	1.483(2)	1.487(2)	1.488(2)	1.494(2)
C$_3$−C$_4$	1.482(3)	1.485(3)	1.482(3)	1.482(2)	1.483(2)	1.487(2)	1.488(2)	1.494(2)
C$_5$−C$_6$	1.480(4)	1.479(4)	1.477(3)	1.478(3)	1.477(2)	1.479(3)	1.484(3)	1.486(3)
C−C$_{av}$	1.481(6)	1.483(6)	1.480(5)	1.481(4)	1.481(3)	1.484(4)	1.487(4)	1.491(4)
r_{AB} [a]	3.632(3)	3.633(3)	3.637(3)	3.639(2)	3.643(2)	3.672(2)	3.707(2)	3.754(2)
Distortion Parameters								
SHAPE (O$_h$)[a]	0.665	0.657	0.646	0.639	0.661	0.726	0.794	0.928
Σ/° [b]	54.4	54.3	54.0	54.0	55.2	58.1	61.0	66.1
Θ/° [b]	177.6	177.3	177.0	177.0	180.7	190.0	198.7	214.3
BVS[d]	3.67	3.65	3.64	3.61	3.60	3.44	3.26	3.02

[a] Average distance (Å) between the three N-C-C-N centroid.[b] *SHAPE* index for octahedral geometry in SHAPE 2.1.[28,29] A value of 0 represents a perfect octahedron.[c] ∑ = sum of the deviation of the 12 N/O−Co−N/O angles from 90°. Θ = sum of the deviation of 24 unique torsional angles between the N/O atoms on opposite triangular faces of the octahedron from 60°, providing the degree of trigonal distortion from an octahedron to trigonal prism. These were calculated using OctaDist[30] - a program for determining the structural distortion of the octahedral complexes. For a perfect octahedron, ∑ and Θ are zero.[d] Bond valence sum.[31,32]

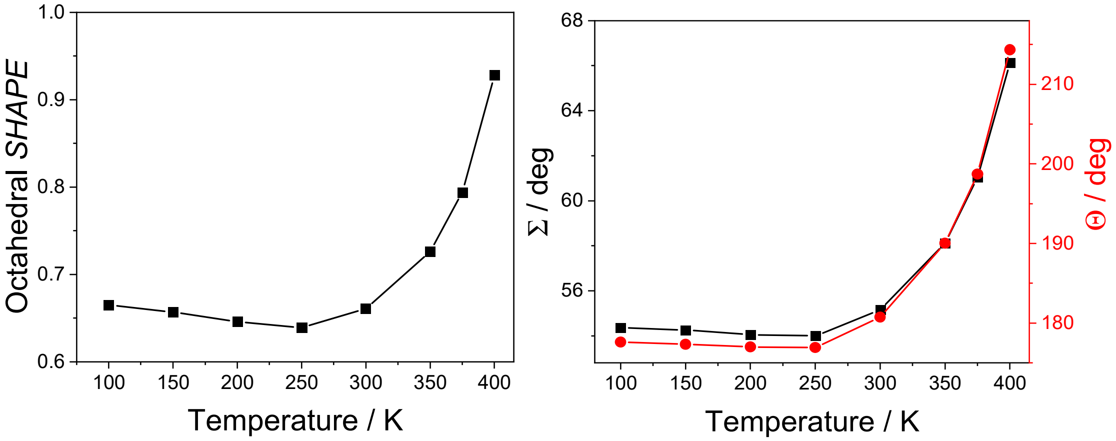

Figure S7. Temperature dependence of the octahedral SHAPE parameter, Σ and Θ distortion parameters for **4**·2*i*Pr$_2$O.

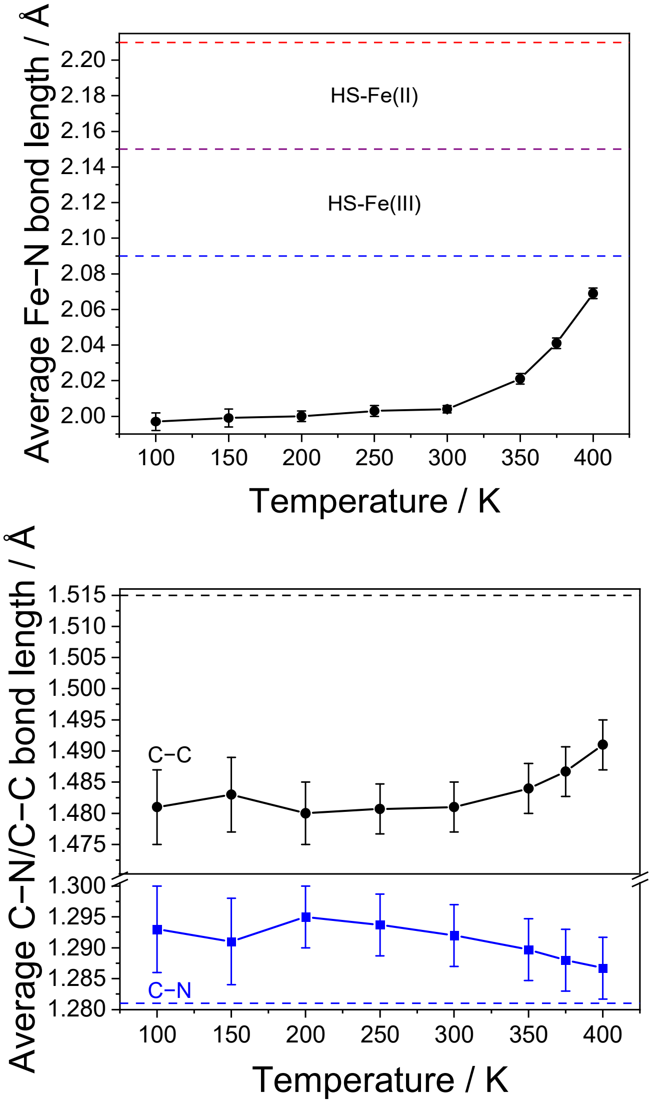

Figure S8. Temperature dependence of the average Fe−N for **4**·2*i*Pr$_2$O vs regions of bond lengths associated with HS-Fe(III) and HS-Fe(II) (dashed lines) (top) and the average C−C and C−N for **4**·2*i*Pr$_2$O vs the average C−C (black dashed line) and C−N (blue dotted line) of **1**·3DCM **2**·DCM·2*i*Pr$_2$O, and **3**·1.5*i*Pr$_2$O.

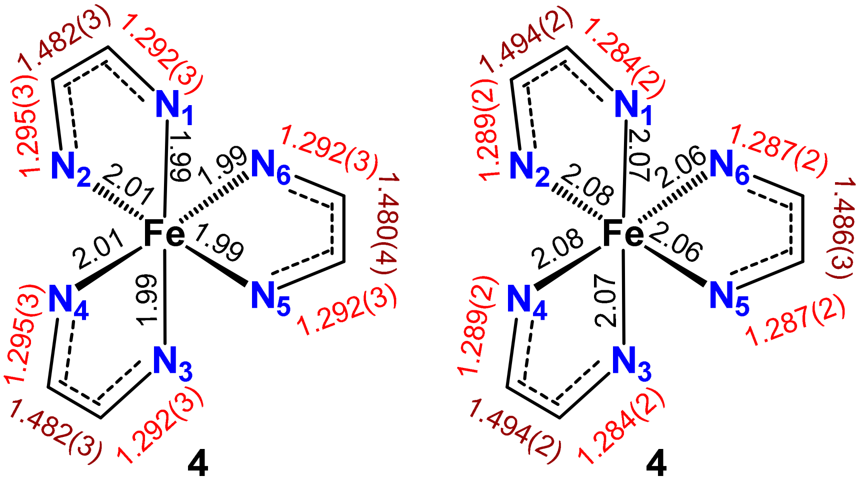

4

Fe-N: 1.997(5) Å
C-N_{av}: 1.293(7) Å
C-C_{av}: 1.481(6) Å

4

Fe-N: 2.070(3) Å
C-N_{av}: 1.287(5) Å
C-C_{av}: 1.491(4) Å

Figure S9. Comparison of bond lengths **4**·2*i*Pr_2O at 100 K (left) and 400 K (right).

Infrared Spectroscopy

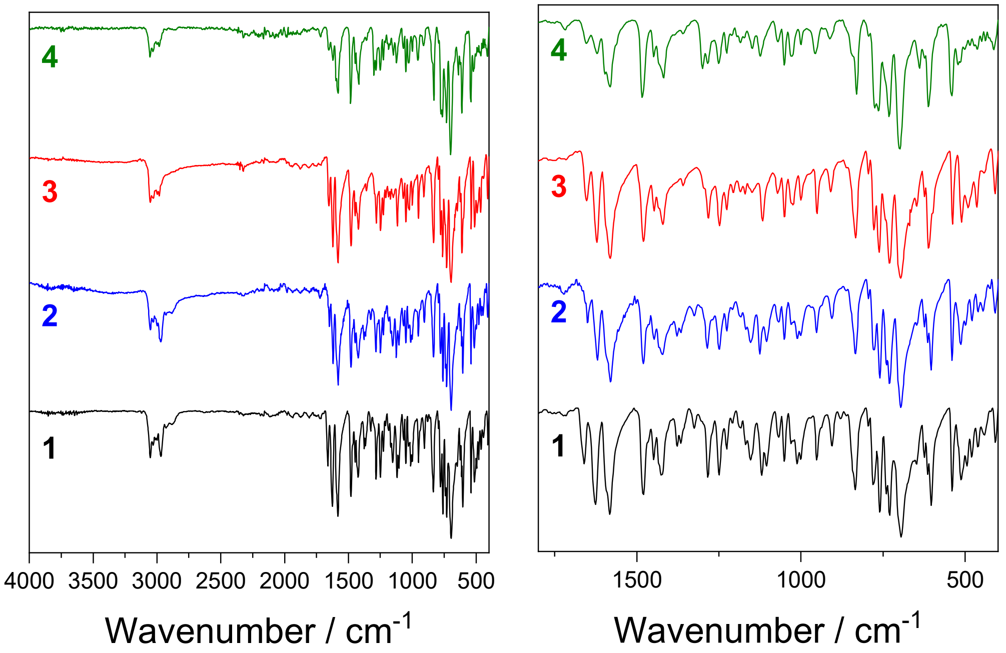

Figure S10. ATR-IR spectra of **1**·1.5DCE·1.5*i*Pr$_2$O, **2**·DCE·1.6*i*Pr$_2$O, **3**·0.4*i*Pr$_2$O and **4**·1.7*i*Pr$_2$O in the region 4000 –400 cm^{-1} (left) and 1800 – 400 cm^{-1} (right).

Solid-State Magnetic Data

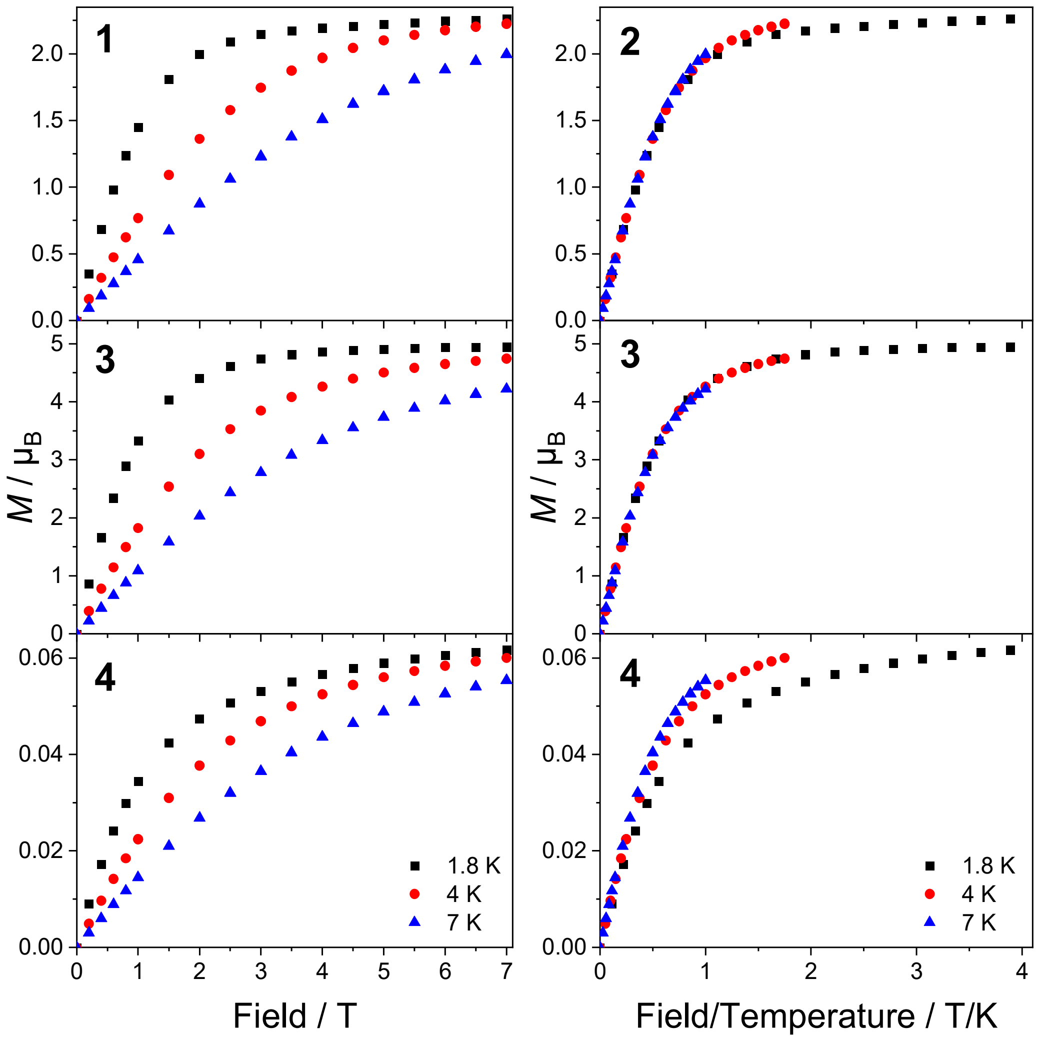

Figure S11. The field dependence of magnetization vs temperature (left) and the plot of magnetization vs field/temperature (right) for **2**·DCE·1.6*i*Pr$_2$O, **3**·0.4*i*Pr$_2$O and **4**·1.7*i*Pr$_2$O at specified temperatures.

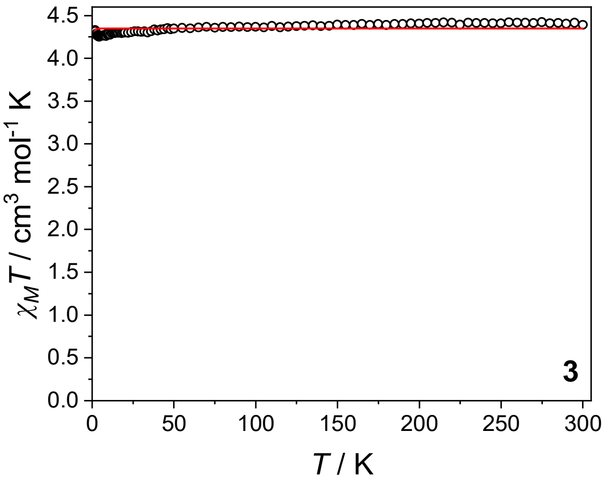

Figure S12. Plot of $\chi_M T$ vs T for **3**·0.3*i*Pr$_2$O (open circles) fit with g = 1.994(1) (red line) using *PHI*.[33]

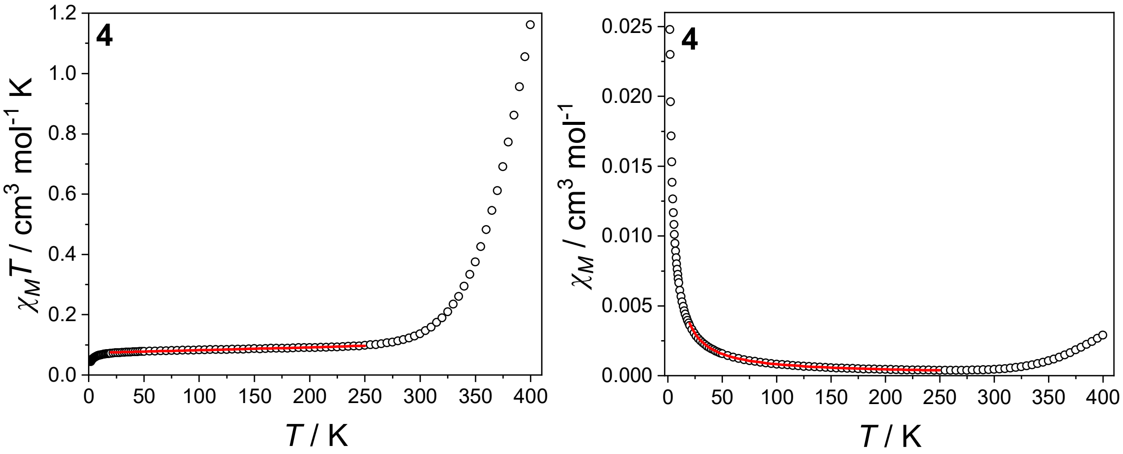

Figure S13. Plot of $\chi_M T$ vs T (left) and χ_M vs T (right) for **4**·1.7*i*Pr$_2$O (open circles) fit with $J = -700(50)$ cm^{-1}, g = 2.00, TIP = $9.4(2)\times10^{-5}$ cm^3 mol^{-1}, 2.4(1)% S = 3/2 HS-Fe(II) impurity (red lines) using PHI.[33]

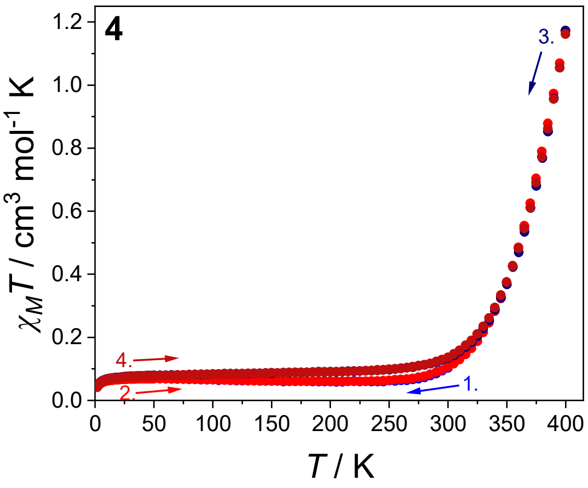

Figure S14. Plots of $\chi_M T$ vs T for **4**·1.7*i*Pr$_2$O on first cooling (blue circles), first heating (red circles), second cooling (dark blue circles) and second heating (dark red circles). Arrows indicate direction and number indicates order of measurement.

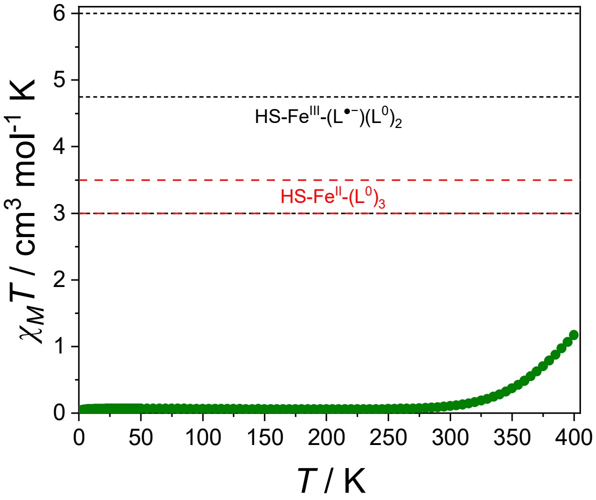

Figure S15. Plots of $\chi_M T$ vs T for **4**·1.7*i*Pr$_2$O on first heating with the dashed red line representing theoretical region of HS-Fe^{II}-(L^0)$_3$ (3.0 – 3.5 cm^3 mol^{-1}) and dotted black line representing theoretical region of HS-Fe^{III}-(L$^{\bullet-}$)(L^0)$_2$ (4.75 – 6.0 cm^3 mol^{-1}).

Photomagnetic Data

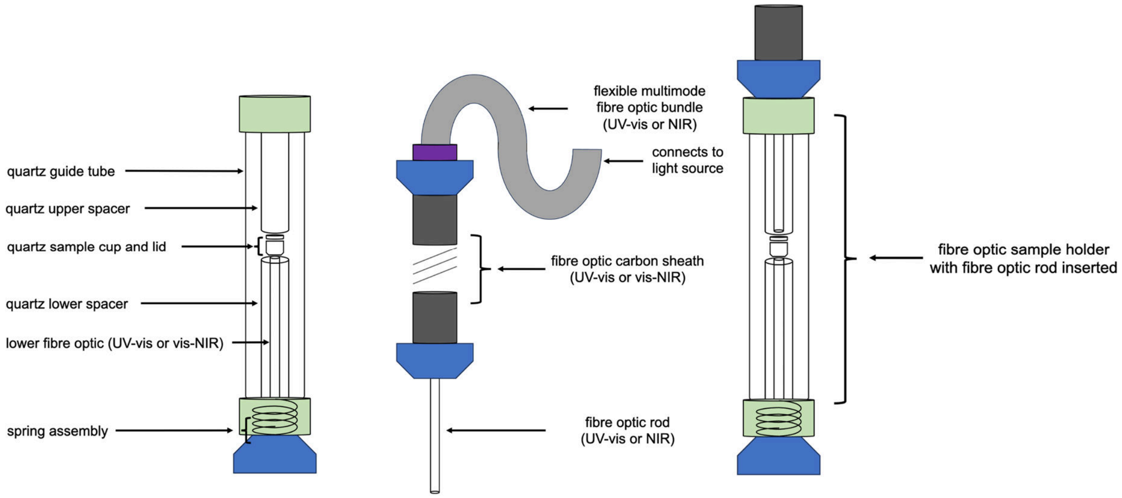

Figure S16. Photomagnetic sample holder schematic, with labelling of each component of the fibre optic sample holder (FOSH) setup.

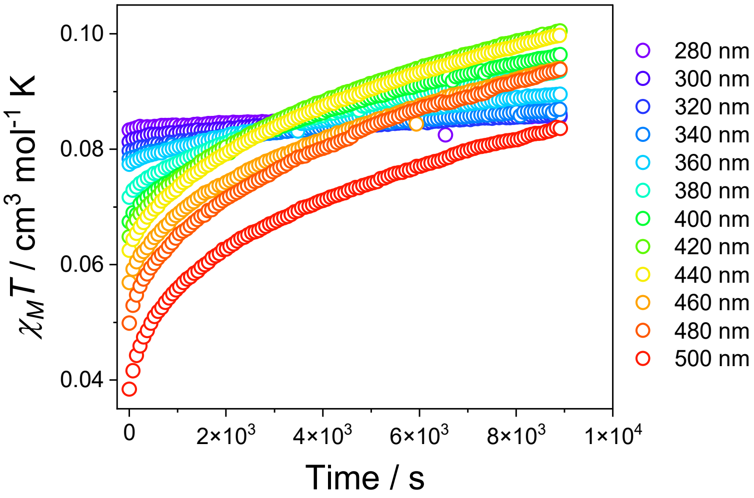

Figure S17. Photomagnetic response of **4**·1.7*i*Pr$_2$O at different irradiation wavelengths at 10 K, plotted as $\chi_M T$ vs Time.

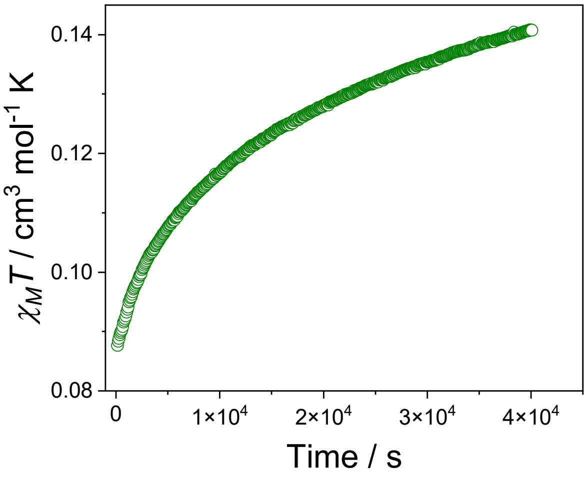

Figure S18. $\chi_M T$ vs Time for **4**·1.7*i*Pr$_2$O after irradiation at 420 nm at 10 K for 12 hours. Note, no photo-stationary point is reached even after 12 hours of continuous irradiation.

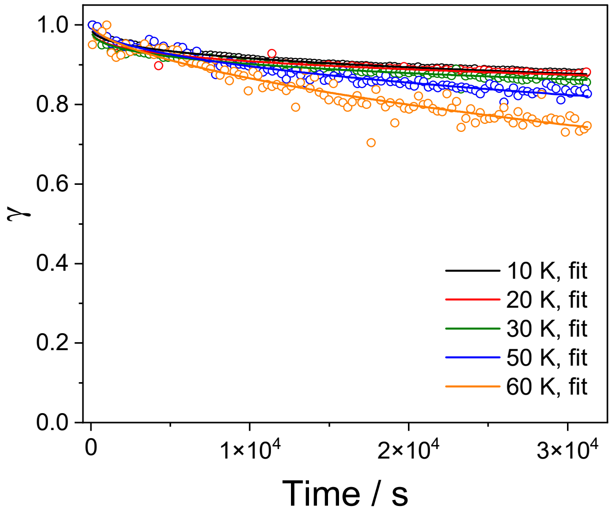

Figure S19. Isothermal relaxation curves of the photoinduced fraction for compound **4**·1.7*i*Pr$_2$O, after 5 hours of 420 nm irradiation at 10 K. The raw data was reduced by averaging every four data points.

Table S5. Parameters obtained from the stretched exponential fits to the relaxation decay curves of compound **4**·1.7*i*Pr$_2$O.

***T* / K**	***τ* / s**	***β***
10	8.41×10^6	0.36
20	2.26×10^7	0.30
30	1.19×10^7	0.32
50	7.18×10^5	0.52
60	2.11×10^5	0.64

Density Functional Theory

Table S6. Spin states (*S*), total energies without (*E*) and with (E^{ZPE}) zero-point harmonic vibrations, relative energies (ΔE), spin density at the metal center (q_s^{M}) and expectation values of the spin-squared operator ($\hat{S}^2$) of the cationic complexes of **2**, **3** and **4** calculated by the DFT UTPSSh/UOPBE/6-311++G(d,p) method.

	Electromer	***S***	***E* (a.u.)**	**E^{ZPE} (a.u.)**	**ΔE (kcal mol^{-1})**	**q_s^{M}**	**$\hat{S}^2$**
2	LS-Co^{II}-(L^0)$_3$	1/2	-4484.473190	-4483.478182	3.8	0.94	0.772
	HS-Co^{II}-(L^0)$_3$	3/2	-4484.479179	-4483.485667	0.0	2.40	3.766
3	HS-Mn^{II}-(L^0)$_3$	5/2	-4252.747236	-4251.754994	0.0	4.61	8.757
	LS-Mn^{II}-(L^0)$_3$	1/2	-4252.738621	-4251.742329	5.4	1.56	0.922
	HS-Mn^{III}-(L$^{\bullet-}$)(L^0)$_2$ BS	3/2	-4252.723245	–	15.1	3.69	4.269
4 UTPSSh	LS-Fe^{II}-(L^0)$_3$	0	-4365.447998	-4364.450691	0.0	0.00	0.000
	IS-Fe^{II}-(L^0)$_3$	1	-4365.424756	-4364.430540	14.6	2.15	2.092
	HS-Fe^{II}-(L^0)$_3$	2	-4365.434053	-4364.441706	8.8	3.65	6.067
	HS-Fe^{III}-(L$^{\bullet-}$)(L^0)$_2$	3	-4365.389070	-4364.397315	37.0	3.98	12.026
4 UOPBE	LS-Fe^{II}-(L^0)$_3$	0	-4364.039577	-4363.053337	2.0	0.00	0.000
	IS-Fe^{II}-(L^0)$_3$	1	-4364.026721	-4363.043426	10.1	2.56	2.352
	HS-Fe^{II}-(L^0)$_3$	2	-4364.042826	-4363.060752	0.0	3.47	6.174
	HS-Fe^{III}-(L$^{\bullet-}$)(L^0)$_2$	3	-4364.003410	-4363.024397	24.7	3.58	12.015

Table S7. Tabulated bond lengths of the geometry optimized electromers of the cationic units of **2** and **3** (UTPSSh/6-311++G(d,p)) with the experimentally determined values.

	Compound 2			**Compound 3**			
	HS-Co^{II}-(L^0)$_3$	**LS-Co^{II}-(L^0)$_3$**	**Exp**	**HS-Mn^{II}-(L^0)$_3$**	**HS-Mn^{III}-(L$^{\bullet-}$)(L^0)$_2$ BS**	**LS-Mn^{II}-(L^0)$_3$**	**Exp**
M–N$_1$	2.179	2.242	2.131(1)	2.286	2.357	2.035	2.262(1)
M–N$_2$	2.175	2.009	2.149(1)	2.285	2.083	2.035	2.242(1)
M–N$_3$	2.174	2.242	2.124(1)	2.288	2.278	2.035	2.263(1)
M–N$_4$	2.176	2.008	2.124(1)	2.284	2.056	2.035	2.283(1)
M–N$_5$	2.178	2.003	2.149(1)	2.286	2.052	2.035	2.268(1)
M–N$_6$	2.179	2.002	2.131(1)	2.288	2.023	2.035	2.275(1)
M−N$_{av}$	2.177	2.085	2.135(1)	2.286	2.147	2.035	2.266(1)
C$_1$−N$_1$	1.291	1.286	1.274(2)	1.289	1.287	1.305	1.287(2)
C$_2$−N$_2$	1.291	1.296	1.285(2)	1.289	1.300	1.305	1.286(2)
C$_3$−N$_3$	1.290	1.286	1.275(2)	1.289	1.295	1.305	1.286(2)
C$_4$−N$_4$	1.291	1.296	1.275(2)	1.289	1.309	1.305	1.285(2)
C$_5$−N$_5$	1.291	1.298	1.285(2)	1.289	1.317	1.305	1.284(2)
C$_6$−N$_6$	1.291	1.298	1.274(2)	1.289	1.318	1.305	1.285(2)
C−N$_{av}$	1.291	1.293	1.278(2)	1.289	1.304	1.305	1.286(2)
C$_1$–C$_2$	1.510	1.507	1.507(2)	1.521	1.513	1.475	1.516(2)
C$_3$–C$_4$	1.511	1.507	1.500(2)	1.521	1.492	1.475	1.520(2)
C$_5$–C$_6$	1.511	1.486	1.507(2)	1.521	1.467	1.475	1.522(2)
C−C$_{av}$	1.511	1.500	1.505(2)	1.521	1.491	1.475	1.519(2)

Table S8. Tabulated bond lengths of the geometry optimized electromers of the cationic units of **4** (UTPSSh/6-311++G(d,p), UOPBE/6-311++G(d,p)) with the experimentally determined values.

	Compound 4 UOPBE					Compound 4 UTPSSh				
	HS-Fe^{II}-(L^0)$_3$	**LS-Fe^{II}-(L^0)$_3$**	**HS-Fe^{III}-(L$^{\bullet-}$)(L^0)$_2$**	**IS-Fe^{II}-(L^0)$_3$**	**Exp**	**HS-Fe^{II}-(L^0)$_3$**	**LS-Fe^{II}-(L^0)$_3$**	**HS-Fe^{III}-(L$^{\bullet-}$)(L^0)$_2$**	**IS-Fe^{II}-(L^0)$_3$**	**Exp**
Fe–N$_1$	2.288	2.011	2.135	1.988	1.991(2)	2.192	2.014	2.197	1.991	1.991(2)
Fe–N$_2$	2.256	2.012	2.136	2.183	2.008(2)	2.197	2.014	2.247	2.155	2.008(2)
Fe–N$_3$	2.191	2.012	2.286	1.988	1.991(2)	2.192	2.013	2.194	2.158	1.991(2)
Fe–N$_4$	2.191	2.012	2.224	2.183	2.008(2)	2.197	2.012	2.242	1.991	2.008(2)
Fe–N$_5$	2.254	2.012	2.285	2.235	1.991(2)	2.226	2.015	2.055	2.187	1.991(2)
Fe–N$_6$	2.281	2.012	2.222	2.235	1.991(2)	2.226	2.014	2.055	2.191	1.991(2)
Fe–N$_{av}$	2.244	2.012	2.215	2.135	1.997(2)	2.205	2.014	2.165	2.112	1.997(2)
C$_1$–N$_1$	1.297	1.308	1.332	1.316	1.292(3)	1.294	1.299	1.291	1.303	1.292(3)
C$_2$–N$_2$	1.297	1.308	1.332	1.305	1.295(3)	1.293	1.299	1.291	1.296	1.295(3)
C$_3$–N$_3$	1.305	1.309	1.302	1.316	1.292(3)	1.294	1.299	1.291	1.296	1.292(3)
C$_4$–N$_4$	1.305	1.308	1.304	1.305	1.295(3)	1.293	1.299	1.291	1.303	1.295(3)
C$_5$–N$_5$	1.297	1.309	1.302	1.297	1.292(3)	1.289	1.299	1.353	1.290	1.292(3)
C$_6$–N$_6$	1.297	1.308	1.305	1.297	1.292(3)	1.289	1.299	1.353	1.290	1.292(3)
C–N$_{av}$	1.300	1.308	1.313	1.306	1.293(3)	1.292	1.299	1.312	1.296	1.293(3)
C$_1$–C$_2$	1.511	1.473	1.461	1.476	1.482(3)	1.507	1.485	1.513	1.489	1.482(3)
C$_3$–C$_4$	1.493	1.473	1.501	1.476	1.482(3)	1.507	1.484	1.514	1.489	1.482(3)
C$_5$–C$_6$	1.511	1.473	1.500	1.502	1.480(4)	1.519	1.484	1.440	1.508	1.480(4)
C–C$_{av}$	1.505	1.473	1.487	1.485	1.481(3)	1.511	1.484	1.489	1.495	1.481(3)

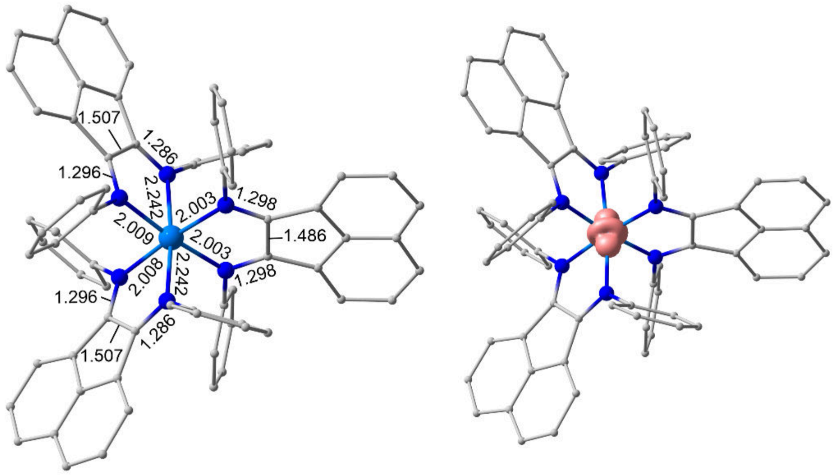

LS-Co^{II}-(L^0)$_3$

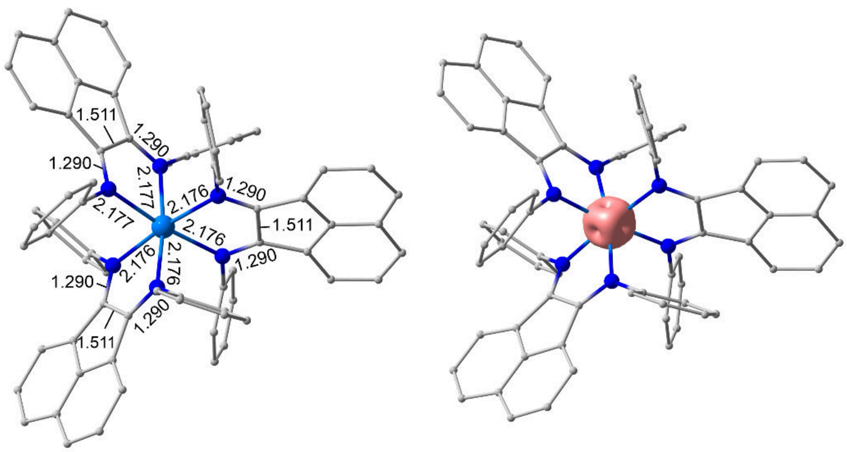

HS-Co^{II}-(L^0)$_3$

Figure S20. Optimized geometries (*left*) and spin density distributions (*right*) in the electromers of **2** calculated by the DFT UTPSSh/6-311++G(d,p) method. Hydrogen atoms are omitted for clarity, bond lengths are given in Å, contour value = 0.02 e Å^{-3}.

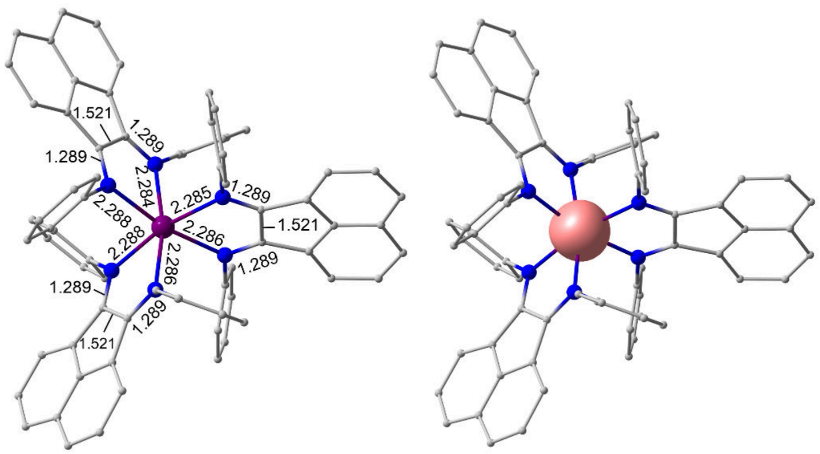

HS-Mn^{II}-$(\text{L}^{0})_{3}$

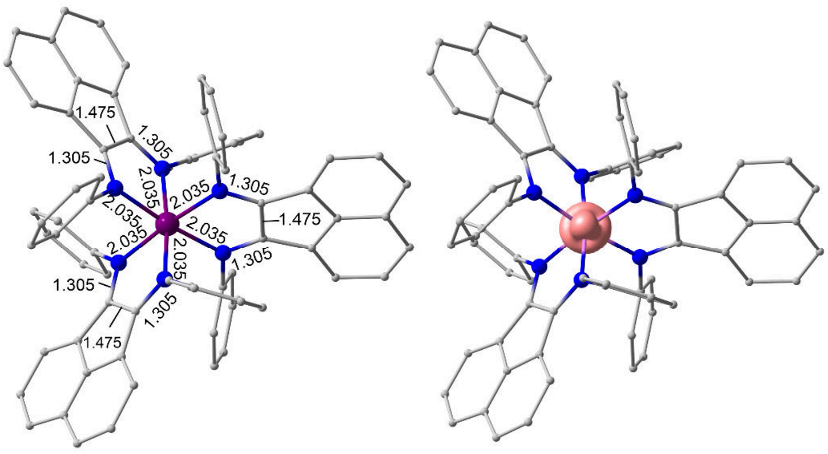

LS-Mn^{II}-$(\text{L}^{0})_{3}$

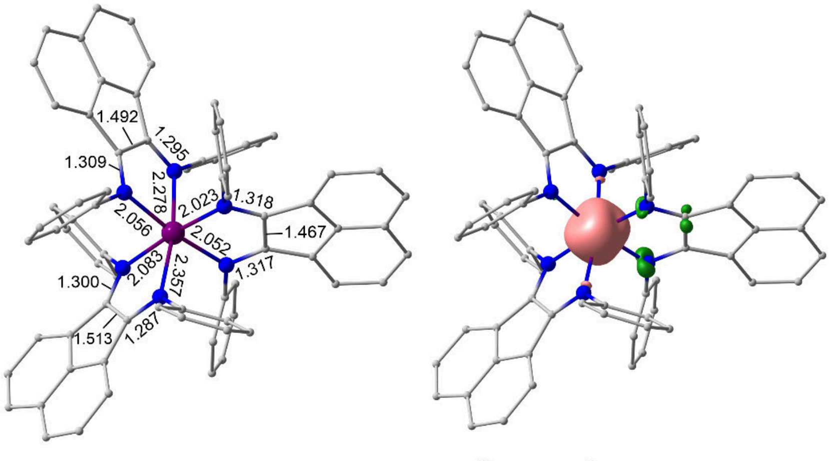

BS state of HS-Mn^{III}-$(\text{L}^{\bullet -})(\text{L}^{0})_{2}$

Figure S21. Optimized geometries (*left*) and spin density distributions (*right*) in the electromers of **3** calculated by the DFT UTPSSh/6-311++G(d,p) method. Hydrogen atoms are omitted for clarity, bond lengths are given in Å, contour value = 0.02 e Å^{-3}.

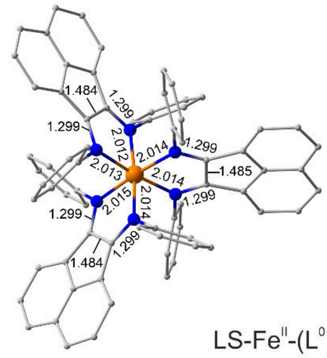

LS-Fe^{II}-(L^0)$_3$

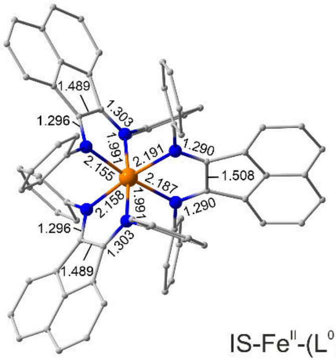

IS-Fe^{II}-(L^0)$_3$

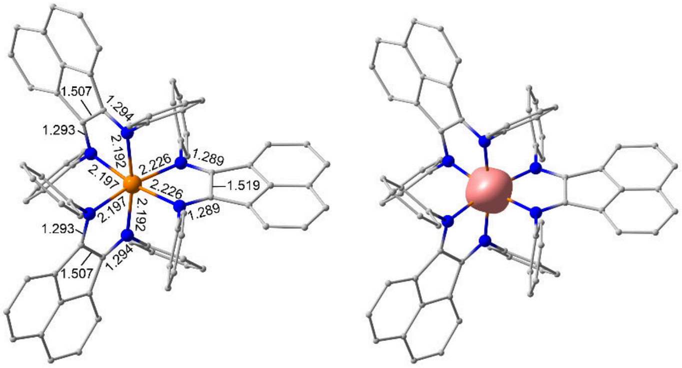

HS-Fe^{II}-(L^0)$_3$

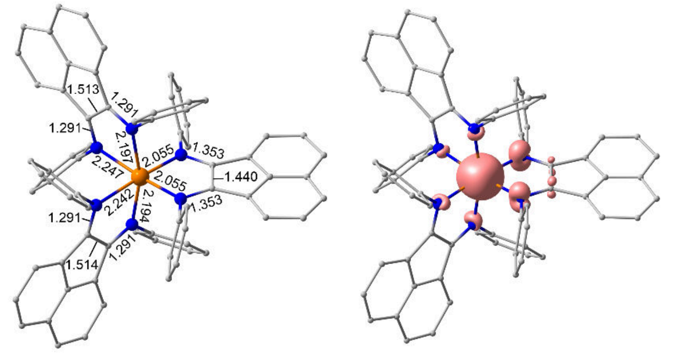

HS-Fe^{III}-(L$^{\bullet -}$)(L^0)$_2$

Figure S22. Optimized geometries (*left*) and spin density distributions (*right*) in the electromers of **4** calculated by the DFT UTPSSh/6-311++G(d,p) method. Hydrogen atoms are omitted for clarity, bond lengths are given in Å, contour value = 0.02 e Å^{-3}.

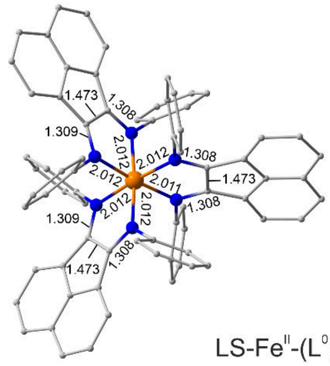

LS-Fe^{II}-(L^{0})$_3$

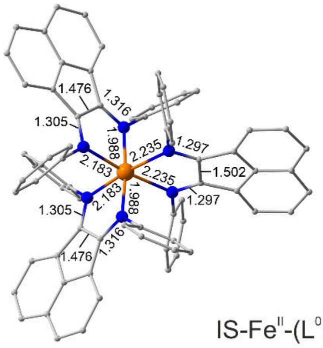

IS-Fe^{II}-(L^{0})$_3$

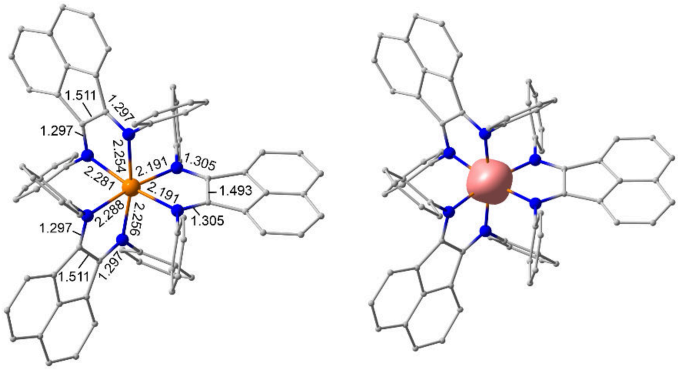

HS-Fe^{II}-(L^{0})$_3$

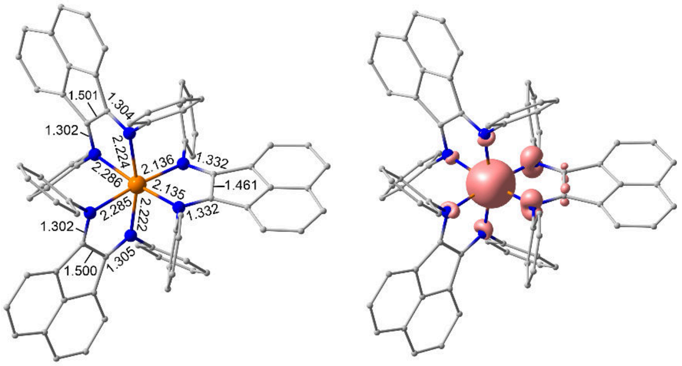

HS-Fe^{III}-(L$^{\bullet -}$)(L^{0})$_2$

Figure S23. Optimized geometries (*left*) and spin density distributions (*right*) in the electromers of **4** calculated by the DFT UOPBE/6-311++G(d,p) method. Hydrogen atoms are omitted for clarity, bond lengths are given in Å, contour value = 0.02 e Å^{-3}.

UV-Vis-NIR Spectroscopy

Table S9. Electronic absorption bands for MeCN, DCE, THF and BuCN solutions and diffuse reflectance of compounds **1**, **2**, **3** and **4**.

Assignment	λ / nm (ε / mol L^{-1} cm^{-1})	Assignment	λ / nm (ε / mol L^{-1} cm^{-1})	Assignment	λ / nm (ε / mol L^{-1} cm^{-1})	Assignment	λ / nm (ε / mol L^{-1} cm^{-1})	Assignment	λ / nm (ε / mol L^{-1} cm^{-1})	Ref
1 (MeCN)		**1** (DCE)		**1** (THF)		**1** (BuCN)		**1** (solid state)		
Ph-BIAN^0 IL	450 (2300), 424 (3800), 400 (4600), 381 (5100)	Ph-BIAN^0 IL	456 (2960), 428 (4770), 406 (5670), 384 (6500)	Ph-BIAN^0 IL	458 (2620), 425 (4600), 404 (5590), 384 (6340)	Ph-BIAN^0 IL	454 (3300), 424 (5810), 400 (7040), 382 (7670)	Ph-BIAN^0 IL	414, 392	10,34
Ph-BIAN^0 IL	324 (25,100)	Ph-BIAN^0 IL	326 (32,400)	Ph-BIAN^0 IL	325 (26,100)	Ph-BIAN^0 IL	325 (35,000)	Ph-BIAN^0 IL	340	10,34
2 (MeCN)		**2** (DCE)		**2** (THF)		**2** (BuCN)		**2** (solid state)		
Ph-BIAN^0 IL	398 (8700)	Ph-BIAN^0 IL	412 (8680)	Ph-BIAN^0 IL	408 (9060)	Ph-BIAN^0 IL	403 (10,600)	Ph-BIAN^0 IL	427	10,34
Ph-BIAN^0 IL	326 (33,700)	Ph-BIAN^0 IL	328 (34,300)	Ph-BIAN^0 IL	328 (34,600)	Ph-BIAN^0 IL	326 (39,000)	Ph-BIAN^0 IL	344	10,34
3 (MeCN)		**3** (DCE)		**3** (THF)		**3** (BuCN)		**3** (solid state)		
Ph-BIAN^0 IL	396 (5800)	Ph-BIAN^0 IL	407 (4100)	Ph-BIAN^0 IL	392 (6000)	Ph-BIAN^0 IL	398 (8000)	Ph-BIAN^0 IL	427	10,34
Ph-BIAN^0 IL	320 (25,800)	Ph-BIAN^0 IL	326 (26,300)	Ph-BIAN^0 IL	304 (21,800)	Ph-BIAN^0 IL	319 (31,000)	Ph-BIAN^0 IL	342	10,34
4 (MeCN)		**4** (DCE)		**4** (THF)		**4** (BuCN)		**4** (solid state)		
IVCT	1540 (410)	IVCT	1564 (130)	IVCT	1558 (2000)	IVCT	1548 (150)			10
LMCT	690 (12,000)	LMCT	695 (17,000)	LMCT	696 (12,100)	LMCT	690 (10,900)	LMCT	704	
Ph-BIAN$^{\bullet-}$ IL	444 (7290), 424 (8280)	Ph-BIAN$^{\bullet-}$ IL	448 (8440), 428 (8820)	Ph-BIAN$^{\bullet-}$ IL	448 (6700), 427 (7290)	Ph-BIAN$^{\bullet-}$ IL	444 (7000), 420 (7910)			35,36
Ph-BIAN^0 IL	418 (8400)	Ph-BIAN^0 IL	428 (8800)	Ph-BIAN^0 IL	424 (7300)	Ph-BIAN^0 IL	420 (7900)	Ph-BIAN^0 IL	430	10,34
Ph-BIAN^0 IL	318 (36,300)	Ph-BIAN^0 IL	321 (35,400)	Ph-BIAN^0 IL	320 (31,900)	Ph-BIAN^0 IL	320 (34,100)	Ph-BIAN^0 IL	339	10,34

Abbreviations: IL = intraligand, LMCT = ligand-to-metal charge transfer, IVCT = intervalence charge transfer

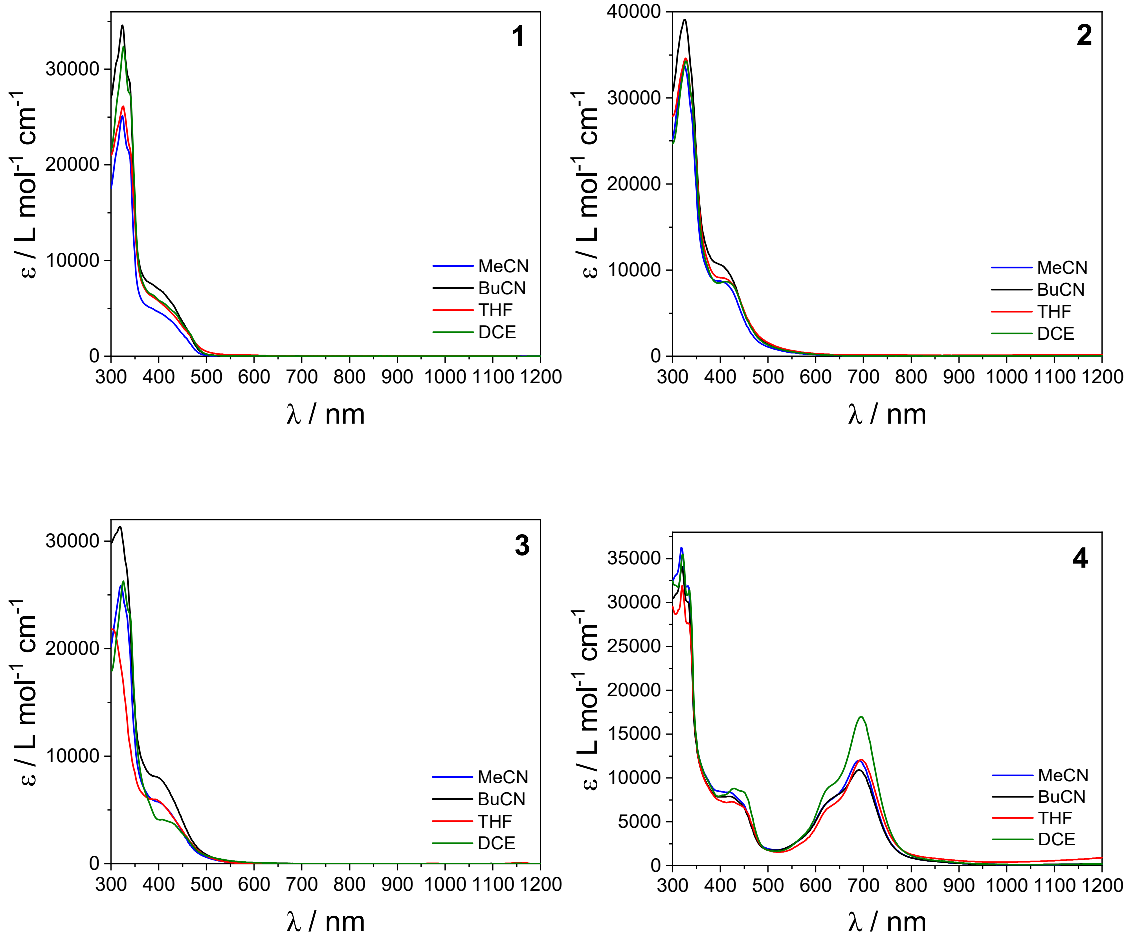

Figure S24. UV-Vis absorption spectra for MeCN, BuCN, THF and DCE solutions of **1**, **2**, **3** and **4** at 298 K.

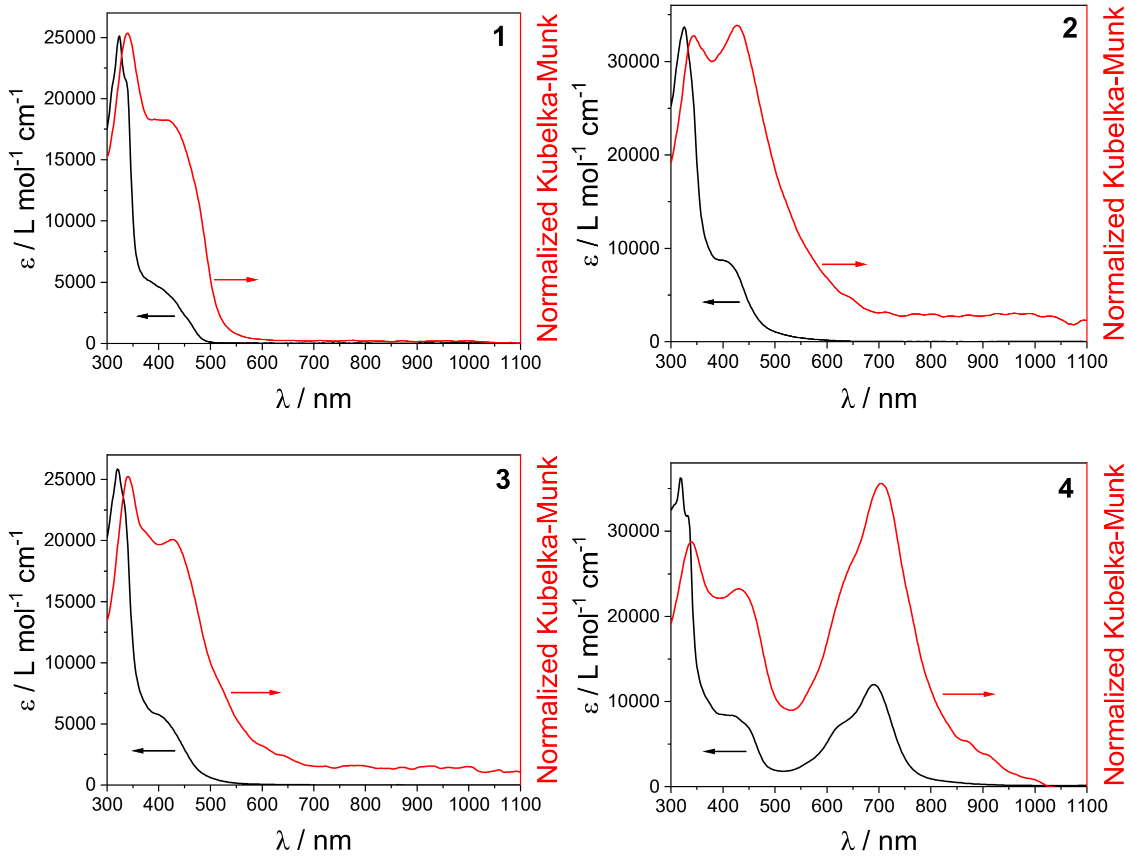

Figure S25. UV-Vis absorption spectra of **1**, **2**, **3** and **4** at room temperature as MeCN solutions (black line) and as diffuse reflectance (diluted ~5% in KBr).

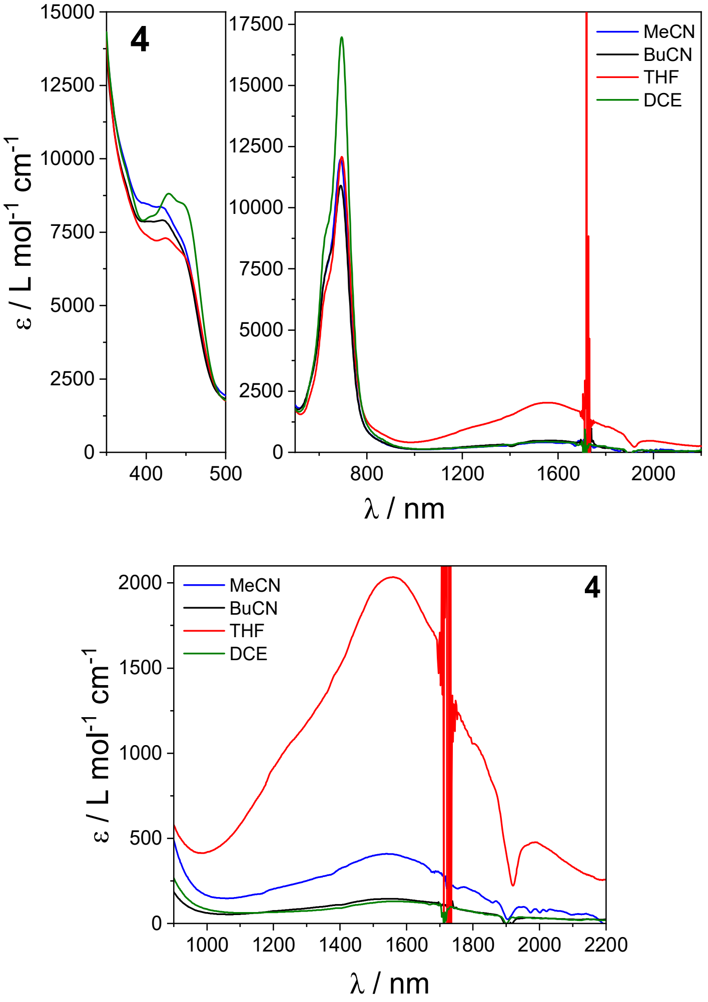

Figure S26. UV-Vis-NIR absorption spectra for MeCN, BuCN, THF and DCE solutions of **4** at 298 K.

Robin-Day Mixed-Valence Classification Analysis

The degree of electronic communication between the Ar-BIAN ligands can be measured by the Robin and Day mixed-valence (MV) class of ligands.[37] Robin-Day Class I mixed-valence systems have a fully localized electronic structure and therefore have no interactions and electron transfer between the centers, with $H_{AB} = 0$ cm^{-1}. Class II corresponds to a localized electronic structure and solvent environment, and as such intervalence charge transfer is intimately linked to the reorganization energy, λ (corrected for the emerging charge delocalization), and which in turn is linked to the energy of the optical charge transfer band ($h\nu_{\max} = \lambda$); for Class II systems $H_{AB} \leq \lambda/2$. There is a non-zero H_{AB} and a IVCT band with energy $h\nu_{\max}$ and full width at half maximum, $\Delta\nu_{1/2}$. The IVCT band for class II are typically solvent-dependent ($\Delta\nu_{\max} > 200$ cm^{-1} for a range of dielectric constant of 30), weak in intensity ($\varepsilon_{max} < 5000$ L mol^{-1} cm^{-1}), broad ($\Delta\nu_{1/2} > 2000$ cm^{-1}), $H_{AB} < 800$ cm^{-1}, and $2H_{AB}/\nu_{\max} \ll 1$.[38–41] As the electronic coupling term increases, the thermal barrier to charge transfer in the ground state decreases, and the system becomes increasingly delocalized. In the limit where there is no ground state barrier to charge transfer, the system moves to Class III, and the coupling term can be simply related to the (solvent independent) IVCT band energy as $2H_{AB} = h\nu_{\max}$, with the IVCT band displaying a pronounced asymmetric shape with a cut-off on the low-energy side. Meyer and colleagues have identified an intermediate case (Class II-III), distinct from the Class II/Class III boundary, in which the redox sites are localized (valence trapped) but electron transfer is faster than the rate of solvent reorganization.[42] This leads to a curious scenario in which the IVCT band offers the symmetric shape associated with Class II, but is not solvatochromic. Class II-III correspond to localized electronic structure and averaged solvent interactions, with $0.7 < 2H_{AB}/\nu_{\max} < 1$, and class III represent electronic and solvent delocalization with $2H_{AB}/\nu_{\max} \gg 1$. Both MV class II-III and III contain IVCT that are solvent independent $\nu_{\max} < 200\ \text{cm}^{-1}$ for a range of dielectric constant of 30), narrow ($\Delta\nu_{1/2} < 2000\ \text{cm}^{-1}$), and intense ($\varepsilon_{max} > 5000$ L mol^{-1} cm^{-1}).[39]

Class II species obey:[42]

$$(\Delta\upsilon_{1/2}°)^2 = 16k_{\mathrm{B}}T\nu_{\mathrm{max}}\ln 2 \qquad \text{(eq. S4)}$$

where $\Delta\nu_{1/2}°$ is the theoretical bandwidth at half maximum (in cm^{-1}), k_{B} is the Boltzmann constant and T is the temperature in K. For a spectrum measured at 298 K, this gives:

$$\Delta\upsilon_{1/2}° = 47.93\sqrt{\nu_{max}} \qquad \text{(eq. S5)}$$

The MV class can be determined by parameter Γ, given by:

$$\Gamma = 1 - (\Delta\upsilon_{1/2})/(\Delta\upsilon_{1/2}°) \qquad \text{(eq. S6)}$$

where $\Gamma < 0.5$ indicate class II, $\Gamma \approx 0.5$ indicate class II-III and $\Gamma > 0.5$ indicate class III.

According to the Hush model,[37,43] H_{AB} can be calculated using:

$$H_{AB} = \frac{2.06\times10^{-2}(\nu_{max}\varepsilon_{max}\Delta\upsilon_{1/2})^{1/2}}{r_{ab}} \qquad \text{(eq. S7)}$$

Where $\varepsilon_{\max}$ (L mol^{-1} cm^{-1}) is the molar absorptivity at $\nu_{\max}$ and r_{AB} is the distance (Å) between the two centers, approximated for **4** as the average distance between the centroids of the three N-C-C-N ($r_{\mathrm{AB}} = 3.632$ Å).[19,41]

Values above the upper limit of H_{AB} correspond to MV class III complexes.

$$H_{ABupper} = \frac{\nu_{max}}{2} \qquad \text{(eq. S8)}$$

The upper limit of **4** for peak 1 is 3199 (MeCN), 3160 (BuCN), 3170 (DCE) and 3150 (THF) cm^{-1}, and for peak 2 is 3860 (MeCN), 3850 (BuCN), 3950 (DCE) and 3800 (THF) cm^{-1}.

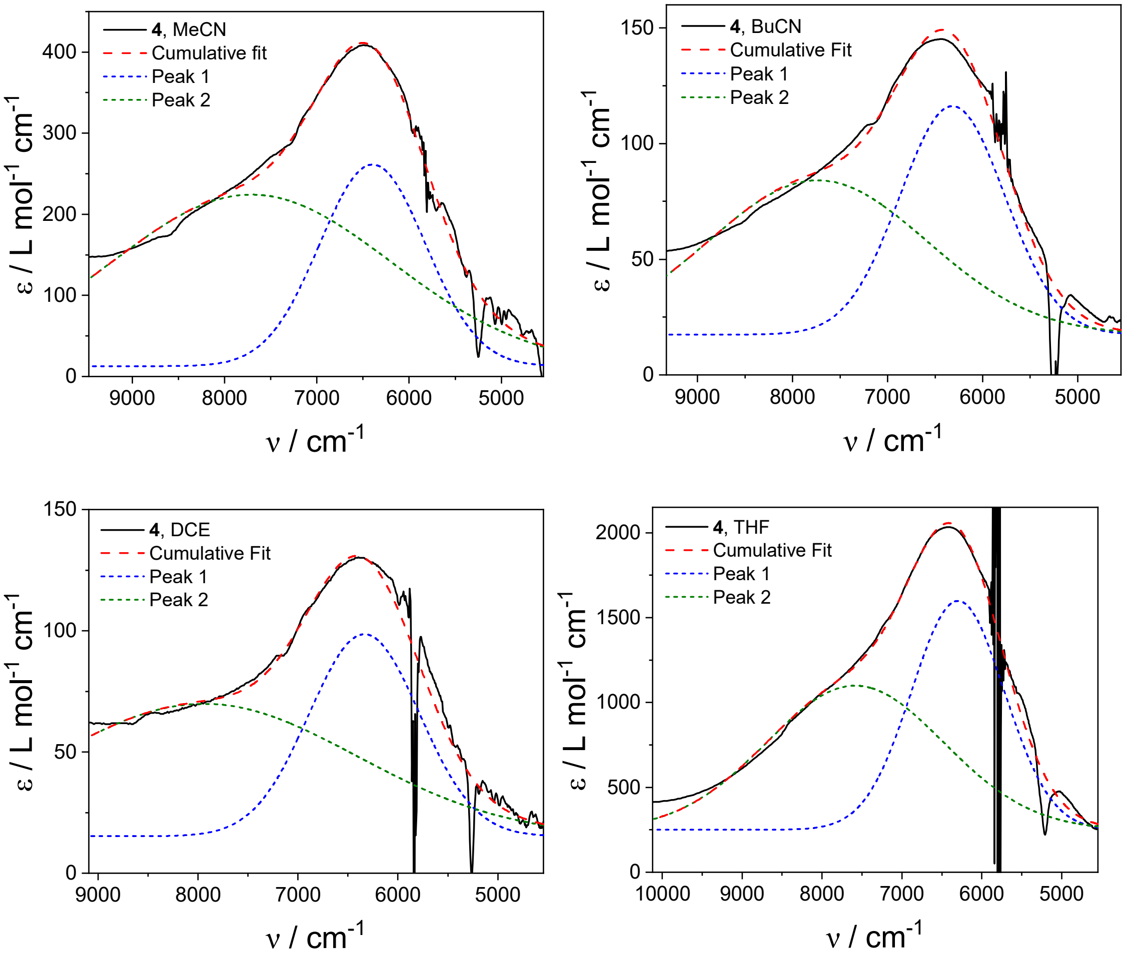

Figure S27. NIR spectrum of **4** in MeCN (top left), BuCN (top right), DCE (bottom left) and THF (bottom right) with a two peak Gaussian fit (MeCN: $R^2 = 0.98$; BuCN: $R^2 = 0.96$; DCE: $R^2 = 0.91$; THF: $R^2 = 0.99$).

Table S10. Mixed-valence and IVCT parameters for **4** in MeCN, BuCN, DCE and THF at 298 K.

	ν_{max} / cm^{-1}	$\Delta\nu_{1/2}$ / cm^{-1}	ε_{max} / L mol^{-1} cm^{-1}	$\Delta\nu_{1/2}°$ / cm^{-1} [a]	Γ [b]	H_{ab} / cm^{-1} [c]	$2H_{AB}/\nu_{max}$
MeCN							
Peak 1	6397(8)	1350(40)	260	3830	0.65	270	0.08
Peak 2	7710(80)	3600(300)	225	4210	0.14	440	0.11
BuCN							
Peak 1	6320(10)	1300(70)	115	3810	0.66	180	0.06
Peak 2	7700(200)	2700(400)	85	4200	0.36	230	0.06
DCE							
Peak 1	6340(10)	1300(90)	100	3820	0.66	160	0.05
Peak 2	7900(200)	4000(1000)	70	4300	0.06	260	0.07
THF							
Peak 1	6299(9)	1370(50)	1600	3800	0.64	670	0.21
Peak 2	7600(200)	2600(300)	1100	4180	0.38	820	0.22

[a] Theoretical bandwidth at half maximum, calculated using equation S4 and S5. [b] Calculated using equation S6. [c] Calculated using equation S7.

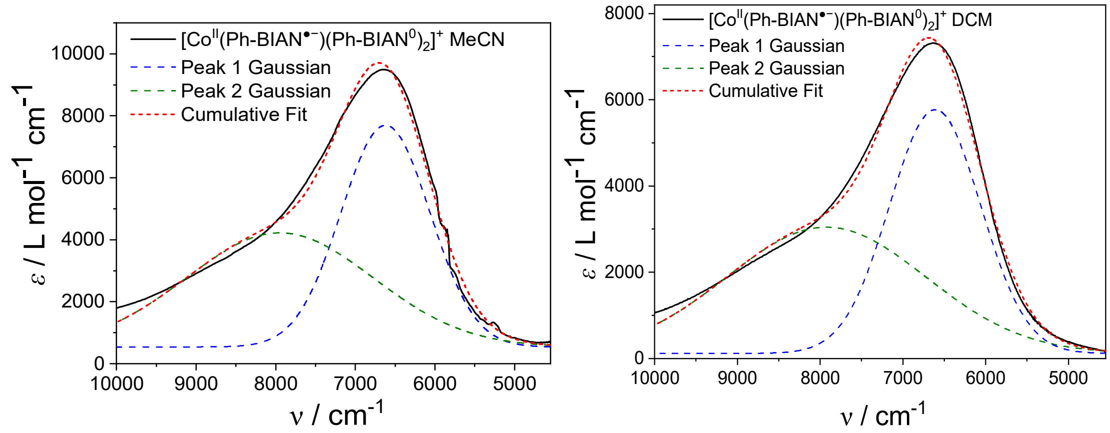

Figure S28. NIR spectrum of $[\mathrm{Co^{II}(Ph\text{-}BIAN^{\bullet-})(Ph\text{-}BIAN^{0})_2}]^+$ in MeCN (left) and DCM (right) with a two peak Gaussian fit (MeCN: $R^2 = 0.99$; DCM: $R^2 = 0.99$).[10]

Table S11. IVCT and mixed-valence parameters for complex $[\mathrm{Co^{II}(Ph\text{-}BIAN^{\bullet-})(Ph\text{-}BIAN^{0})_2}]^+$

	$\nu_{\max}$ / cm^{-1}	$\Delta\nu_{1/2}$ / cm^{-1}	$\varepsilon_{\max}$ / L mol^{-1} cm^{-1}	$\Delta\nu_{1/2}^{\circ}$ / cm^{-1} [a]	Γ [b]	H_{ab} / cm^{-1} [c]	$2H_{AB}/\nu_{\max}$
MeCN							
Peak 1	6622(3)	1320(20)	7700	3900	0.66	1380	0.42
Peak 2	7950(70)	2800(100)	4200	4270	0.34	1630	0.41
DCM							
Peak 1	6610(2)	1310(10)	5700	3900	0.66	1190	0.36
Peak 2	7930(30)	2830(30)	2200	4270	0.34	1190	0.30

[a] Theoretical bandwidth at half maximum, calculated using equation S4 and S5. [b] Calculated using equation S6. [c] Calculated using equation S7.

Variable Temperature UV-Vis Spectroscopy

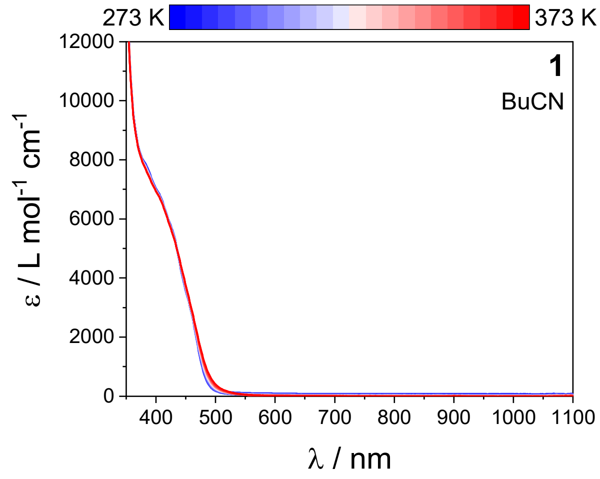

Figure S29. Variable temperature absorption spectra of **1** in BuCN between 273 and 373 K, in 5 K increments.

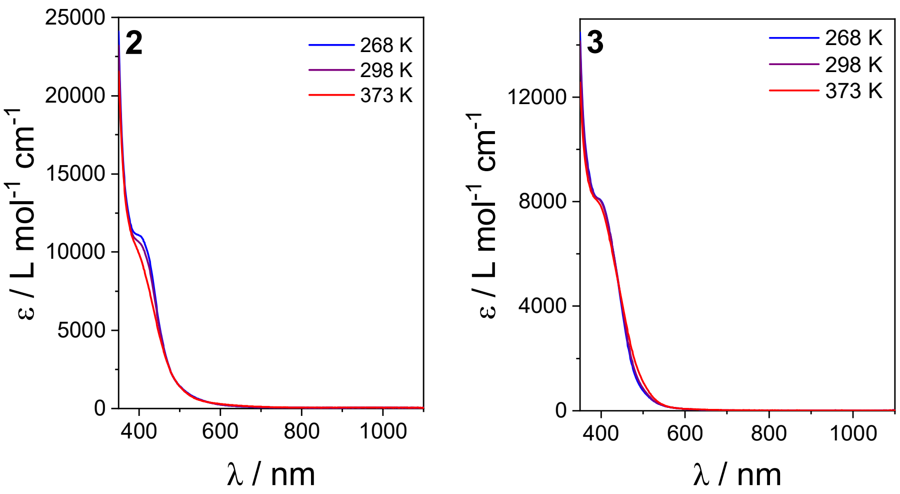

Figure S30. Variable temperature absorption spectra of **2** and **3** in BuCN at specified temperatures.

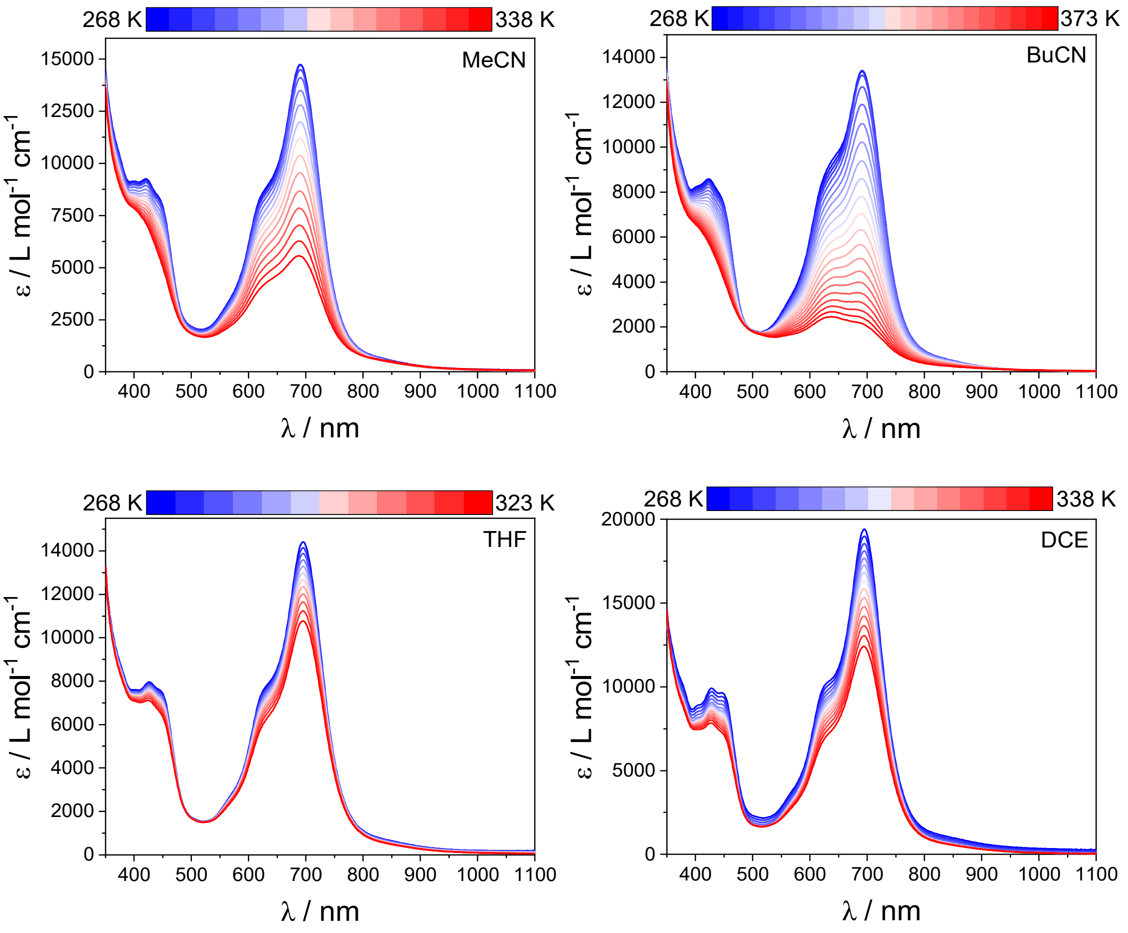

Figure S31. Variable temperature absorption spectra of **4** in MeCN (268 – 338 K), BuCN (268 – 373 K), THF (268 – 323 K), and DCE (268 – 338 K) in 5 K increments.

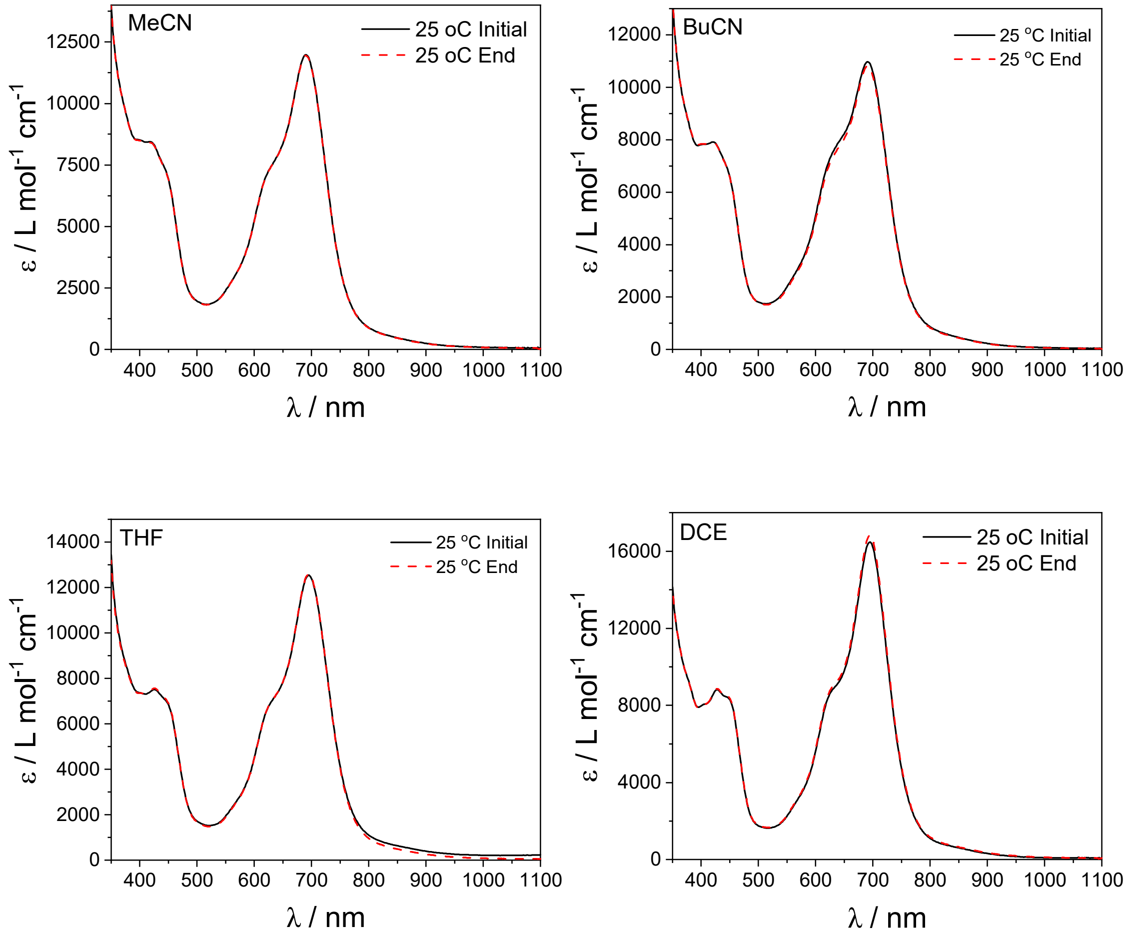

Figure S32. UV-Vis sample of **4** in MeCN, BuCN, THF and DCE at 298 K measured immediately following dissolution (black solid line) and after heating from 268 to 338 K (MeCN), 373 K (BuCN), 323 K (THF) or 338 K (DCE) (red dashed line).

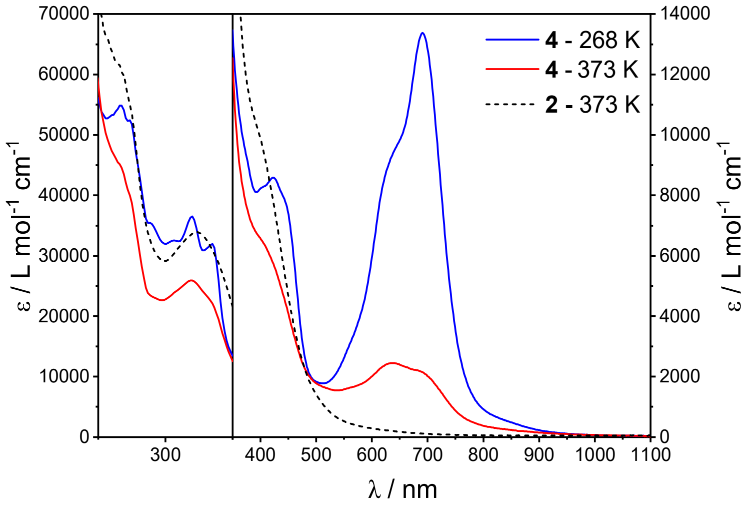

Figure S33. UV-Vis spectra of **4** at 268 and 373 K vs UV-Vis spectrum of **2** at 373 K in BuCN.

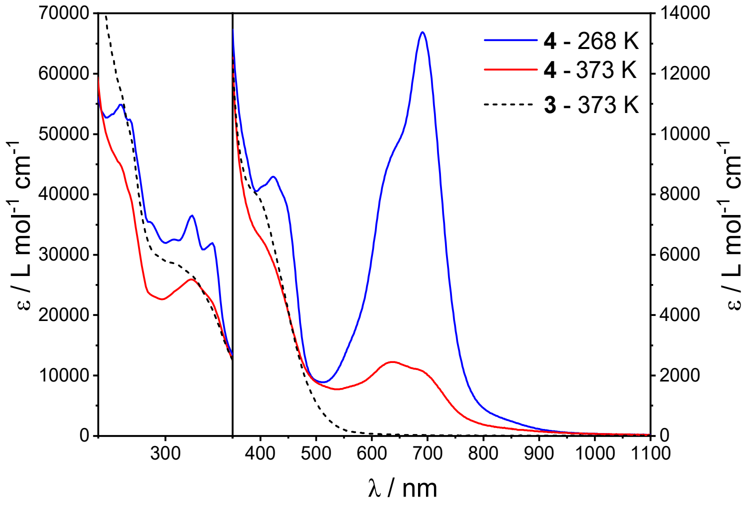

Figure S34. UV-Vis spectra of **4** at 268 and 373 K vs UV-Vis spectrum of **3** at 373 K in BuCN.

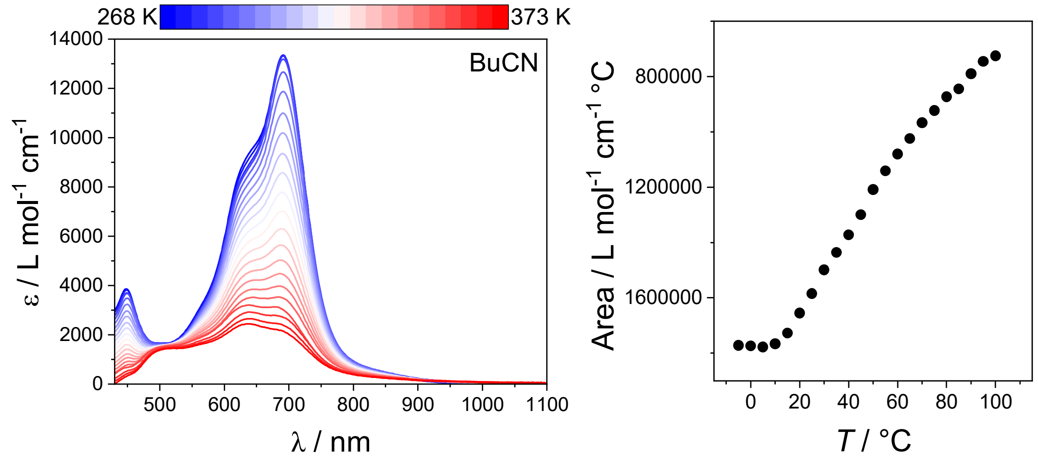

Figure S35. UV-Vis spectra of **4** between 268 – 373 K with subtraction of the UV-Vis spectra of **1** in BuCN at the same corresponding temperature (left). Plot of the relative area of the deconvoluted UV-Vis spectra of **4** (left in figure) vs temperature.

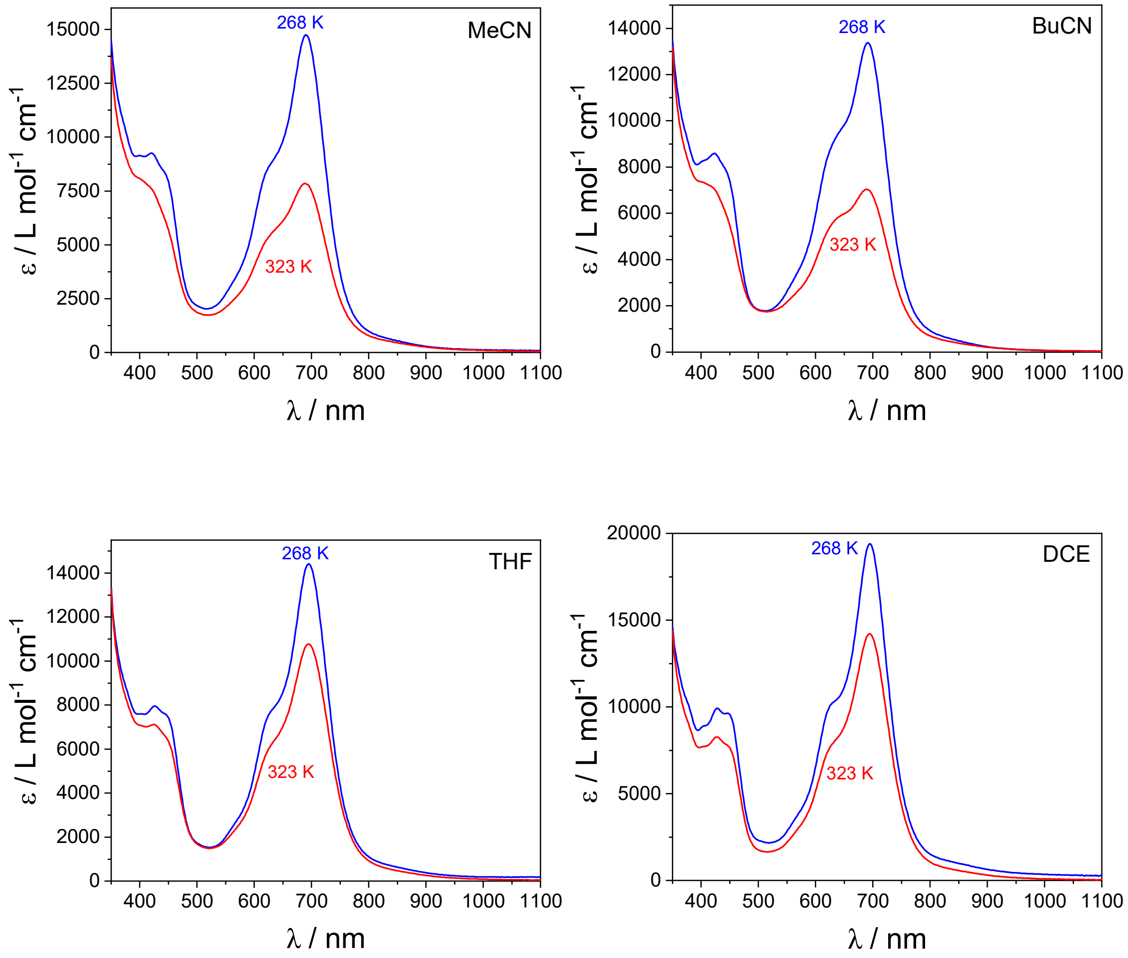

Figure S36. UV-vis spectra of **4** in MeCN, BuCN, THF, and DCE at 268 K (blue) and 323 K (red) highlighting degree of spectra change.

Solution-State Magnetic Measurements

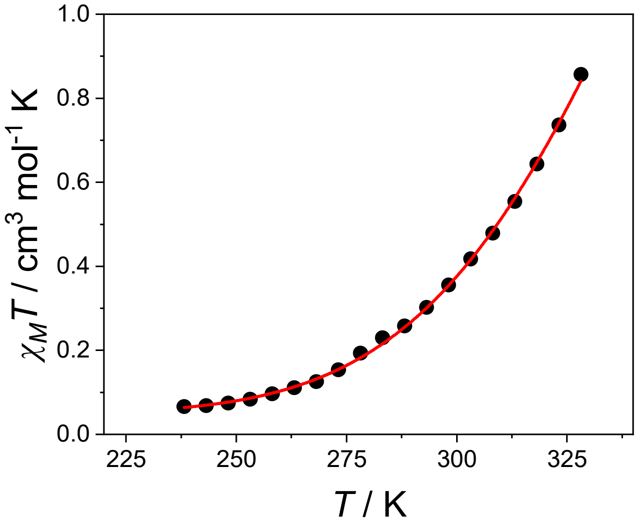

Figure S37. Plots of $\chi_M T$ vs T for **4** in MeCN with a regular solution model fit (red line) (R^2 = 0.999).

Electrochemistry

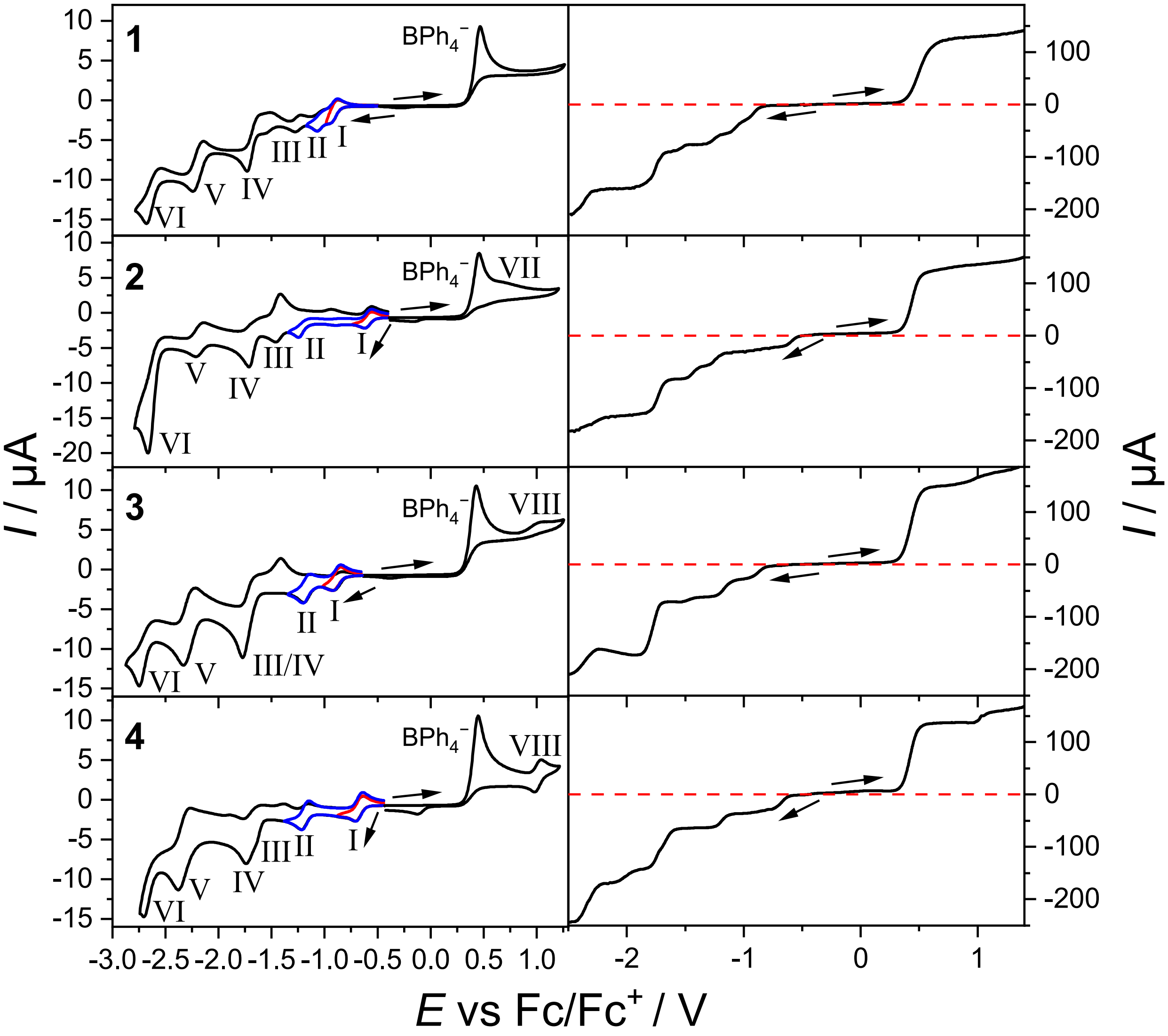

Figure S38. Cyclic voltammograms of MeCN solutions of compounds **1**, **2**, **3** and **4** (1.0 mM with 0.25 M Bu_4NPF_6) obtained with a scan rate of 100 mV s^{-1} (left). Corresponding RDE voltammograms at a scan rate of 50 mV s^{-1} and a rotation rate of 500 rotations min^{-1} (right). Arrows indicate the starting point and direction of the scan.

References

1 A. Cimino, F. Moscatelli, F. Ferretti, F. Ragaini, S. Germain, J. Hannedouche, E. Schulz, L. Luconi, A. Rossin and G. Giambastiani, *New J. Chem.*, 2016, **40**, 10285–10293.

2 D. Aragão, J. Aishima, H. Cherukuvada, R. Clarken, M. Clift, N. P. Cowieson, D. J. Ericsson, C. L. Gee, S. Macedo, N. Mudie, S. Panjikar, J. R. Price, A. Riboldi-Tunnicliffe, R. Rostan, R. Williamson and T. T. Caradoc-Davies, *J. Synchrotron Radiat.*, 2018, **25**, 885–891.

3 N. P. Cowieson, D. Aragao, M. Clift, D. J. Ericsson, C. Gee, S. J. Harrop, N. Mudie, S. Panjikar, J. R. Price, A. Riboldi-Tunnicliffe, R. Williamson and T. Caradoc-Davies, *J. Synchrotron. Radiat.*, 2015, **22**, 187–190.

4 Rigaku Oxford Diffraction. CrysAlisPro version 1.171.40.14a, Rigaku Corporation, Wroclaw (Poland), 2018.

5 G. M. Sheldrick, SADABS, University of Göttingen, Germany, 1996.

6 G. M. Sheldrick, *Acta Crystallogr., Sect. A: Found. Adv.*, 2015, **71**, 3–8.

7 G. M. Sheldrick, *Acta Crystallogr., Sect. C: Struct. Chem.,* 2015, **71**, 3–8.

8 O. V. Dolomanov, L. J. Bourhis, R. J. Gildea, J. A. K. K. Howard and H. Puschmann, *J. Appl. Crystallogr.*, 2009, **42**, 339–341.

9 P. van der Sluis and A. L. Spek, *Acta Crystallogr., Sect. A: Found. Adv.*, 1990, **46**, 194–201.

10 M. A. Hay, J. T. Janetzki, V. J. Kumar, R. W. Gable, R. Clérac, A. A. Starikova, P. J. Low and C. Boskovic, *Inorg. Chem.*, 2022, **61**, 17609–17622.

11 *Wissoft 2003*; Wissenschaftliche Elektronik GmbH: Ortenberg, Germany, 2010.

12 Lagarec, K.; Rancourt, D. G. *Recoil 1.05 – Mössbauer spectral analysis software for Windows*; Department of Physics, University of Ottawa, Canada, 1998.

13 D. F. Evans, *J. Chem. Soc.*, 1959, 2003–2005.

14 S. Brahma and R. L. Gardas, *J. Mol. Liq.*, 2018, **256**, 22–28.

15 S. O. Morgan and H. H. Lowry, *J. Phys. Chem.*, 1930, **34**, 2385–2432.

16 G. A. Bain and J. F. Berry, *J. Chem. Educ.*, 2008, **85**, 532.

17 J. Tao, J. P. Perdew, V. N. Staroverov and G. E. Scuseria, *Phys. Rev. Lett.*, 2003, **91**, 146401.

18 V. N. Staroverov, G. E. Scuseria, J. Tao and J. P. Perdew, *J. Chem. Phys.*, 2003, **119**, 12129–12137.

19 G. K. Gransbury, B. N. Livesay, J. T. Janetzki, M. A. Hay, R. W. Gable, M. P. Shores, A. Starikova and C. Boskovic, *J. Am. Chem. Soc.*, 2020, **142**, 10692–10704.

20 T. Tezgerevska, E. Rousset, R. W. Gable, G. N. L. Jameson, E. C. Sañudo, A. Starikova and C. Boskovic, *Dalton Trans.*, 2019, **48**, 11674–11689.

21 J. Cirera, M. Via-Nadal and E. Ruiz, *Inorg. Chem.*, 2018, **57**, 14097–14105.

22 O. S. Siig and K. P. Kepp, *J. Phys. Chem. A*, 2018, **122**, 4208–4217.

23 Y. Hitomi, M. Higuchi, H. Minami, T. Tanaka and T. Funabiki, *Chem. Commun.*, 2005, 1758–1760

24 J. T. Janetzki, M. G. Chegerev, G. K. Gransbury, R. W. Gable, J. K. Clegg, R. J. Mulder, G. N. L. Jameson, A. A. Starikova and C. Boskovic, *Inorg. Chem.*, 2023, **62**, 15719–15735.

25 M. G. Chegerev and A. A. Starikova, *Comput. Theor. Chem.*, 2022, **1211**, 113693.

26 J. Sirirak, D. Sertphon, W. Phonsri, P. Harding and D. J. Harding, *Int. J. Quantum Chem.*, 2017, **117**, 1–8.

27 M. Swart, *J. Chem. Theory. Comput.*, 2008, **4**, 2057–2066.

28 S. Llunell, M. Casanova, D. Cirera, J. Alemany and P. Alvarez, SHAPE 2.1, 2013.

29 S. Alvarez, D. Avnir, M. Llunell and M. Pinsky, *New J. Chem.*, 2002, **26**, 996–1009.

30 R. Ketkaew, Y. Tantirungrotechai, P. Harding, G. Chastanet, P. Guionneau, M. Marchivie and D. J. Harding, *Dalton Trans.*, 2021, **50**, 1086–1096.

31 P. H. C. Camargo, *J. Mater. Sci.*, 2017, **52**, 9959–9962.

32 I. D. Brown and D. Altermatt, *Acta Crystallogr., Sect. B: Struc. Sci., Crys. Eng., Mat.*, 1985, **244**, 244–247.

33 N. F. Chilton, R. P. Anderson, L. D. Turner, A. Soncini and K. S. Murray, *J. Comput. Chem.*, 2013, **34**, 1164–1175.

34 V. L. Nadurata, M. A. Hay, J. T. Janetzki, G. K. Gransbury and C. Boskovic, *Dalton Trans.*, 2021, **50**, 16631–16646.

35 I. L. Fedushkin, A. A. Skatova, V. A. Chudakova, V. K. Cherkasov, G. K. Fukin and M. A. Lopatin, *Eur. J. Inorg. Chem.*, 2004, 388–393.

36 I. L. Fedushkin, A. A. Skatova, M. Hummert and H. Schumann, *Eur. J Inorg. Chem.*, 2005, 1601–1608.

37 P. Robin and Melvin B. Day, *Adv. Inorg. Chem. Radiochem.*, 1967, **10**, 247–422.

38 D. M. D'Alessandro and F. R. Keene, *Chem. Soc. Rev.*, 2006, **35**, 424–440.

39 A. Arnold, T. J. Sherbow, R. I. Sayler, R. D. Britt, E. J. Thompson, M. T. Muñoz, J. C. Fettinger and L. A. Berben, *J. Am. Chem. Soc.*, 2019, **141**, 15792–15803.

40 K. Tahara, T. Kadowaki, J. Kikuchi, Y. Ozawa, S. Yoshimoto and M. Abe, *Bull. Chem. Soc. Jpn.*, 2018, **91**, 1630–1639.

41 Á. Moneo, G. C. Justino, M. F. N. N. Carvalho, M. C. Oliveira, A. M. M. Antunes, D. Bléger, S. Hecht and J. P. Telo, *J. Phys. Chem. A*, 2013, **117**, 14056–14064.

42 K. D. Demadis, C. M. Hartshorn and T. J. Meyer, *Chem. Rev.*, 2001, **101**, 2655–2685.

43 N. S. Hush, *Electrochim. Acta*, 1968, **13**, 1005–1023.